DROP ELECTROHYDRODYNAMICS

A Thesis

Presented to the Faculty of the Graduate School

of Cornell University

in Partial Fulfillment of the Requirements for the Degree of

Master of Science

by

Alejandro Agustín Carderera de Diego

August 2016

ABSTRACT

Electrohydrodynamics is the study of the interaction between fluids and electric fields, and is used to model phenomena like fuel atomization or the mixing of multiphase flows under the influence of electric fields.

Increasing interest is being placed in using electric fields to vary multiphase behaviour, one example is combustion processes, where finer droplets and wider sprays are created to increase engine efficiency. Another example can be seen in the pharmaceutical industry, where micro-encapsulation of compounds is achieved through the use of electrified coaxial liquid jets.

In this work, the Ghost Fluid Method (GFM), and the Continuum Surface Force (CSF) approach will be used to discretize the electric potential Poisson equation for multiphase problems with arbitrary interfaces and discontinuous physical properties. A new scheme has also been derived to solve this problem, in the Finite Volume (FV) framework, and an extensive error analysis has been carried out to gauge the accuracy and properties of these schemes.

These tools, coupled with NGA, the Computational Fluid Dynamics (CFD) code used in Dr. Olivier Desjardins' research group will allow the study of, among others, the two phase mixing of two dielectric liquids under the influence of an electric field, of interest to the chemical engineering industry, where an alternative non-mechanical way of mixing corrosive liquids is sought out, or the atomization of drops during fuel injection when an electric field is applied.

BIOGRAPHICAL SKETCH

Alejandro Carderera earned his Bachelors Degree in Industrial Engineering Technologies in 2014 from the Universidad Politécnica de Madrid (Escuela Técnica Superior de Ingenieros Industriales). He joined the Master of Science program in Applied and Engineering Physics at Cornell University in August 2014.

His interest in CFD sparked during his last year of undergraduate study, in which he was granted a Research Collaboration Scholarship by the Spanish Ministry of Education to conduct research in the department of fluid mechanics under the guidance of Dr. Jaime Carpio. This work formed the base of his undergraduate thesis, which aimed at improving current methods to solve CFD problems with mobile frontiers in the Finite Element Method (FEM) framework, and later allowed him to study the freefall regimes of circular discs according to their corresponding Froude and Reynolds number.

As a graduate student at Cornell University, he joined the Computational Thermo-Fluids Laboratory in August of 2015, undertaking research in electrohydrodynamics (EHD) supervised by Dr. Olivier Desjardins.

This document is dedicated to my family, Kala, my friends and to my supervisor, Professor Olivier Desjardins.

ACKNOWLEDGEMENTS

I would like to thank my advisor Olivier for his untiring guidance during this project, as well as for the myriad of brilliant suggestions and advice that have led to this document and its content.

A number of students have been instrumental or inspirational in the development of my research and among these are Robert Chiodi, Peter Ireland, Ravi Patel, John Palmore, Houssen Kasbaoui, Stephanie Firehammer, Sheng Wang and Meilin Dong.

This thesis would not have been possible without the help, support and patience of my family, Kala and my friends, as well as to all the people who have mentored and counselled me, which include Ruth Siboza and Dr. Jaime Carpio.

TABLE OF CONTENTS

LIST OF TABLES

LIST OF FIGURES

CHAPTER 1

INTRODUCTION

1.1 Background and motivation

The electric stresses inherent to EHD are being used by engineers and researchers worldwide to raise the efficiency of jet and automotive engines by better atomizing the fuel under ever-stricter environmental regulations, or to create novel micrometer pharmaceutical emulsions by generating minuscule droplets in a controlled fashion.

Drop behaviour is key in the understanding of these phenomena, and further efforts need to be made in order to elucidate the exact impact of electric stresses in the onset of fluid turbulence and atomization processes. Substantial progress has been made in the past decade towards the accurate simulation of these systems, but work still needs to be done to be able to accurately model three dimensional multiphase electrohydrodynamics.

This work aims at characterizing the tools used to model the dynamic behaviour of drops immersed in fluids subjected to strong uniform DC electric fields. More specifically, the Poisson discretization that is used to model these systems.

1.2 Previous Work

1.2.1 Experimental and theoretical work

In the late nineteenth century Lord Rayleigh studied the equilibrium conditions of a charged quiescent drop [1], in an article considered by most as the departing point for the study of the interaction between electric fields and fluid flows.

Three decades later, in 1909, Robert A. Millikan and Harvey Fletcher performed the famous oil drop experiment, in which they determined the charge of an electron by applying an electric field between two parallel plates on a drop in equilibrium, where the electrical force and gravitational force where balanced.

Drawing from the experiments of J. Zeleny, who photographed cone jets of dielectric liquids ejected out of a capillary [2], and others like Wilson [3], Nolan [4] and Macky [5], G.I. Taylor [6] provided a theoretical explanation of the physics behind the phenomena observed. He provided an explanation to the oblate shape of dielectric drops in dielectric media, the prolate shape of conducting drops in dielectric media and the electrically driven conical jet shapes observed through a capillary, which are named Taylor cones.

Another incremental effort in the understanding of electrohydrodynamics was made by R. Allan and S. Mason [7], who studied fluids that were neither perfect conductors nor perfect dielectrics, but poorly conducting liquids, known as leaky dielectrics. G.I. Taylor constructed a model to explain their behaviour, which was further developed later on by J.R. Melcher [8]. An excellent review of this model (also known as the Taylor-Melcher model) can be found in

the article by D.A. Saville [9]

It was thanks to the insight of G.I. Taylor [6] that the behaviour of a drop of dielectric liquid immersed in a non-conducting dielectric fluid, subject to a weak DC electric field was understood. This drop will maintain a spheroidal shape only if the electric stresses are balanced by a variable pressure difference between the inside and outside of the drop. This will only be possible if the fluids inside and outside of the drop are in motion, due to the accumulation of steady currents at the interface. This spheroidal flow configuration was calculated, and a condition on the properties of the two liquids was established to determine whether a spherical drop would be possible or not, in the seminal paper by Taylor [10]. When these conditions are not verified, the drop forms either an oblate or prolate ellipsoid, whose shape can be predicted depending on a ratio that takes into account electrical stress and surface tension.

As the electric field is increased, an interesting phenomenon is observed, the non-axisymmetric rotational behaviour of the particle. This system closely resembles the rotation of solid dielectric particles, observed by Quincke in the 19th century. In contrast to the latter, the liquid drop is affected by drop size and by the ratio of viscosities, given by $\lambda = \mu_{in}/\mu_{ext}$, due to the effect of charge convection along the interface by the straining EHD flow. The key parameters that are used to determine the rotation are the threshold electric field E_C, at which the drop commences its rotation, the tilt angle that the major axis of the drop presents with the electric field β and the angular velocity ω.

Both of these behaviours can be considered as Stokes flow, due to the prevalence of viscosity over inertia ($Re << 1$). The first drop configuration corresponds to the application of weak electric fields, studied analytically by Tay-

lor [10], with which Vhlahovska's and Salipante's experiments show good results [11, 12]. In this first case, the parameter of interest is the oblate/prolate drop deformation, which can be quantified by,

$$D = \frac{d_{\parallel} - d_{\perp}}{d_{\parallel} + d_{\perp}} = \frac{9R_0\epsilon_{ex}E_0^2}{16\gamma S(2+R)^2} f(R,S,\lambda), \tag{1.1}$$

Where $d_{\parallel}$ and $d_{\perp}$ are the diameter lengths of the drop parallel and perpendicular to the electric field direction respectively, R_0 is the radius of the drop, γ is the surface tension coefficient, $R = \sigma_{in}/\sigma_{ex}$ is the ratio of conductivities, $S = \epsilon_{in}/\epsilon_{ex}$ is the ratio of permittivities, $\lambda = \mu_{in}/\mu_{ex}$ is the ratio of viscosities and $f(R,S,\lambda)$ is a function of R, S and λ. In this case, the two competing forces of interest are the electrical stresses and surface tension, which can be quantified using the appropriate time scales t_{EHD} and t_{γ}, which can be used to form the following capillary number,

$$t_{EHD} = \frac{\mu_{ex}(1-\lambda)}{\epsilon_{ex}E_0^2}, \tag{1.2}$$

$$t_{\gamma} = \frac{\mu_{ex}(1-\lambda)a}{\gamma}, \tag{1.3}$$

$$Ca_{EHD} = \frac{t_{\gamma}}{t_{EHD}} = \frac{a\epsilon_{ex}E_0^2}{\gamma}. \tag{1.4}$$

The experiments show accordance with the analytical formula for the deformation, up until $Ca = 0.2$ after which the experimental results diverge from the theory, as was shown by Vizika [13].

Regarding the second set-up where drop rotation is studied, the previous capillary number is also relevant, but a new ratio of time-scales arises, given by the ratio of the time it takes for charge to be convected by rotation, given by the Maxwell-Wagner polarization time scale t_{MW} and the surface tension time scale t_{γ}, which leads to

$$t_{MW} = \frac{\epsilon_{in} + 2\epsilon_{ex}}{\sigma_{in} + 2\sigma_{ex}}, \tag{1.5}$$

$$Ca_{MW} = \frac{t_\gamma}{t_{MW}} = \frac{a\sigma_{ex}\mu_{ex}}{\epsilon_{ex}\gamma}\frac{S(R+2)(\lambda+1)}{1+2S}. \tag{1.6}$$

The deviation of the behaviour of drop rotation with respect to Quincke rotation (regarding the dependence of drop shape and viscosity) can be explained by considering the charging of the surface with charges from the fluid bulk and the movement of those charges via the drop rotation. Characterized by

$$Re_E = \frac{t_{c,ex}}{t_{EHD}} = Ca\frac{t_{c,ex}}{t_\gamma} \simeq \frac{Ca}{Ca_{MW}}, \tag{1.7}$$

where the coefficient Re_E represents the electric Reynolds number, which is the ratio of the charging time-scale from the bulk fluid and the time-scale of the EHD phenomenon.

Regarding the effect of parameter variation in the system, Salipante et al. [11], showed that as we decrease the drop size and the viscosity ratio, the threshold field E_C is increased, with a greater viscosity dependence.

1.2.2 Numerical work

Oguz et al. [14] numerically studied in 1997 the process by which gas bubbles grow in an underwater orifice, using a potential flow boundary integral formulation. The model developed was capable of tackling axisymmetric, as well as three dimensional problems, but suffered from numerical instabilities, as is common with boundary integral methods, even though an damping term was introduced to mitigate them.

A year later in 1998 Sherwood [15] used a boundary integral technique to model the axisymmetric time dependent low Reynolds number deformation of droplets in electric and magnetic fields. The scheme obtained the deformation

of the drop by utilising energy minimization arguments, in which the sum of the bulk electrical and surface energy of the spheroidal drop mas minimized.

Baygents et al. [16] also utilised integral equation methods to model the electric and velocity fields in the domain, allowing them to study the axisymmetric interaction of drops of the same size. The leaky dielectric model, developed by G.I. Taylor was used to simulate a range of conductivities and permittivities, showing good agreement with the prolate and oblate predictions of Taylor's model.

Higuera [17] further extended in 2006 the work of Oguz [14], simulating the injection and coalescense of bubbles in the with and without and electric field, considering that in the latter case there was no shear stress at the surface of the drop due to the absence of charge accumulation at the interface.

A year later, Collins et al. [18] studied the injection of a perfectly conducting liquid under the influence of an electric field, thereby modelling Laplace's equation instead of Poisson's equation. In this paper, two different schemes were employed, the first one being an axisymmetric Galerkin Finite Element Method (FEM) to solve the Navier-Stokes and Laplace's equation, and a hybrid Galerkin FEM that related the one-dimensional thin jet to the axisymmetric representation of the field.

In that same year, Tomar et al. [19] employed a coupled level set and volume-of-fluid (CLSVOF) method to track the interface and the Continuum Surface Force (CSF) approach to smear out the effects of the electric field at the fluid interface. Two different regimes are investigated, given by highly conducting and highly insulating liquids, and in both of these, the effects of the

electric and fluid coupling is only felt at the fluid interface. In both of these situations weighted harmonic averaging is used to interpolate properties to the interface. This numerical approach, in axisymmetric coordinates, allows then to accurately reproduce the behaviour of spherical and spheroidal drops, and the interaction between pairs of drops, although a fine mesh is required to obtain good results.

CHAPTER 2

MATHEMATICAL MODEL

2.1 Navier Stokes Equations

The governing equations used for the description of the multiphase flow are the following.

2.1.1 Conservation of Mass

The underlying physical principle states that mass cannot be created or destroyed, which must be verified for each phase being considered. Here α will be used to denote these phases ($\alpha = l$ for liquid and $\alpha = g$ for gas).

$$\frac{\partial \rho_\alpha}{\partial t} + \nabla \cdot (\rho_\alpha \mathbf{u}_\alpha) = 0, \tag{2.1}$$

where ρ is the density and $\mathbf{u}_\alpha$ is the velocity. This equation is also known as the continuity equation, due to the fact that the only requisites that need to be verified for this equation to be true are the continuity of ρ_α and $\mathbf{u}_\alpha$. Due to the incompressible nature of the flow, this equation simplifies to:

$$\nabla \cdot \mathbf{u}_\alpha = 0. \tag{2.2}$$

Thus the velocity is solenoidal.

2.1.2 Conservation of Momentum

The underlying physical principle states that the time rate of change of momentum of a body equals the net force exerted on it, expressed in conservative form as

$$\frac{\partial \rho_\alpha \mathbf{u}_\alpha}{\partial t} + \nabla \cdot (\rho_\alpha \mathbf{u}_\alpha \otimes \mathbf{u}_\alpha) = \nabla \cdot \boldsymbol{\tau}_\alpha + \mathbf{f}_\alpha. \tag{2.3}$$

This equation can be written in the non-conservative form using conservation of mass.

$$\frac{\partial \rho_\alpha \mathbf{u}_\alpha}{\partial t} + (\rho_\alpha \mathbf{u}_\alpha \cdot \nabla)\, \mathbf{u}_\alpha = \nabla \cdot \boldsymbol{\tau}_\alpha + \mathbf{f}_\alpha, \tag{2.4}$$

where $\boldsymbol{\tau}_\alpha$ is the stress tensor and $\mathbf{f}_\alpha$ are the body forces acting on the fluid. The stress tensor represents surface forces, of which we will distinguish three types, pressure, viscous and electrohydrodynamic forces, i.e.,

$$\boldsymbol{\tau}_\alpha = -p_\alpha \mathbb{1} + \boldsymbol{\sigma}_\alpha + \boldsymbol{\sigma}_\alpha^{ehd}, \tag{2.5}$$

where p_α is the pressure, $\boldsymbol{\sigma}_\alpha$ is the viscous stress tensor, and $\boldsymbol{\sigma}_\alpha^{ehd}$ is the Maxwell stress tensor, which links the electrostatic field to the fluid dynamics of the problem. The former is given by,

$$\boldsymbol{\sigma}_\alpha = \mu_\alpha \left(\nabla \mathbf{u}_\alpha + \nabla \mathbf{u}_\alpha^{\mathsf{T}} \right) - \frac{2}{3} \mu_\alpha \nabla \cdot \mathbf{u}_\alpha \mathbb{1}, \tag{2.6}$$

where μ_α is the dynamic viscosity of the fluid. Due to the solenoidal nature of the velocity field, the last term of the viscous stress tensor will be zero.

The Maxwell stress tensor, of which detailed derivations can be found in Landau, Melcher and Stratton [20–22], is expressed mathematically as

$$\boldsymbol{\sigma}_\alpha^{ehd} = \epsilon \mathbf{E}\mathbf{E} - \frac{\epsilon}{2} \epsilon \mathbf{E} \cdot \mathbf{E} \left(1 - \frac{\rho}{\epsilon} \frac{\partial \epsilon}{\partial \rho} \right) \mathbb{1}, \tag{2.7}$$

where ϵ represents the permittivity of the material and $\mathbf{E}$ the electric field. The divergence of this tensor, which is involved in Eq. 2.4, is known as the electric

force density, which we will denote as $\mathbf{f}^{ehd}$.

$$\mathbf{f}^{ehd} = q\mathbf{E} - \frac{1}{2}\mathbf{E}^2\nabla\epsilon + \nabla\left\{\frac{1}{2}\rho\frac{\partial\epsilon}{\partial\rho}\mathbf{E}^2\right\}, \tag{2.8}$$

in which q represents the charge density in the given fluid. The three terms found in Eq. 2.8 represent the Coulombic force, the dielectric force and the electrostrictive force. Due to homogeneity of ϵ in the fluids, the only non-zero term will be the Coulomb contribution, leaving us with

$$\nabla \cdot \boldsymbol{\sigma}^{ehd} = \mathbf{f}^{ehd} = q\mathbf{E}. \tag{2.9}$$

2.2 Electromagnetic Equations

The governing equations which will determine the behaviour of the system are Maxwell's equations:

$$\nabla \cdot \mathbf{D} = q, \tag{2.10}$$

$$\nabla \cdot \mathbf{B} = 0, \tag{2.11}$$

$$\nabla \times \mathbf{E} = -\frac{\partial \mathbf{B}}{\partial t}, \tag{2.12}$$

$$\nabla \times \mathbf{B} = \mu_0\left(\mathbf{J} + \epsilon_0\frac{\partial \mathbf{B}}{\partial t}\right), \tag{2.13}$$

where $\mathbf{B}$ is the magnetic flux density, $\mathbf{J}$ is the electric current density, and ϵ_0 and μ_0 is the permittivity and the permeability of vacuum respectively. Due to the fact that we will be making the electrostatic assumption, and thus the time derivatives of $\mathbf{E}$ and $\mathbf{B}$ will be taken to be null, we will be able to decouple the equations into the magnetostatic equations and the electrostatics equations. Focusing only on the latter, since $\mathbf{E}$ is irrotational, it derives from a potential ϕ, i.e.,

$$\mathbf{E} = -\nabla\phi, \tag{2.14}$$

Therefore, we can rewrite Eq. 2.10 as

$$\nabla \cdot \mathbf{D} = \nabla \cdot (\epsilon \mathbf{E}) = \nabla \cdot (-\epsilon \nabla \phi) = q, \tag{2.15}$$

which due to the homogeneity of ϵ in the fluids leads to

$$\triangle \phi = -\frac{q}{\epsilon}, \tag{2.16}$$

which will be referred from now on as the *electric potential Poisson equation*.

2.3 Interface Conditions

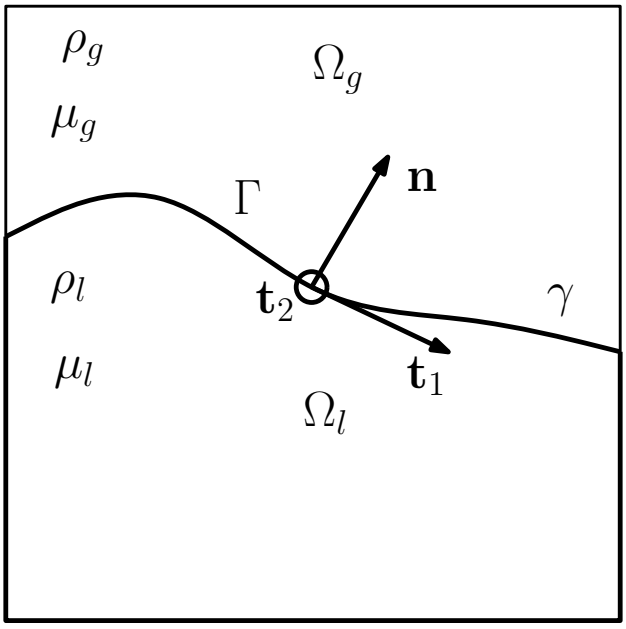

Figure 2.1: Multiphase interface configuration.

Consider the configuration depicted in Fig. 2.1, where we have defined a reference frame relative to the interface Γ separating the two fluids, where $\mathbf{n}$ represents the interphase normal and $\mathbf{t}_1$ and $\mathbf{t}_2$ represent the two vectors tangent

to Γ. We will employ brackets to denote interphase jump conditions, such that for the quantity a,

$$[a]_\Gamma = a_l - a_g. \tag{2.17}$$

For a vector quantity, such as $\mathbf{A}$, we will represent the jump in the tangential component as $[\mathbf{A} \cdot \mathbf{t}]_\Gamma$ or $[\mathbf{A}_t]_\Gamma$, and the jump in the normal component as $[\mathbf{A} \cdot \mathbf{n}]_\Gamma$ or $[\mathbf{A}_n]_\Gamma$.

As is obvious, material properties linked to a specific fluid experience the following jumps.

$$[\rho]_\Gamma = \rho_l - \rho_g, \tag{2.18}$$

$$[\epsilon]_\Gamma = \epsilon_l - \epsilon_g, \tag{2.19}$$

$$[\mu]_\Gamma = \mu_l - \mu_g. \tag{2.20}$$

Velocity Continuity

Due to the fact that the interface acts as a material surface, mass conservation dictates that there must not be any mass transfer between the phases.

$$[\mathbf{u} \cdot \mathbf{n}]_\Gamma = 0. \tag{2.21}$$

The viscous nature of the flow that we are considering leads us to *assume* the continuity of the tangential component of the velocity at the interface, i.e.,

$$[\mathbf{u} \cdot \mathbf{t}_i]_\Gamma = 0 \quad \text{for} \quad i = 1, 2. \tag{2.22}$$

Electrostatic Jump Conditions

The application of Gauss's law in Eq. 2.10 in integral form to a differential Gaussian pillbox enclosing part of the interface, as found in Griffiths [23], leads to the

following interface condition for the electric displacement:

$$\oint \mathbf{D} \cdot d\mathbf{S} = Q_{enc}, \tag{2.23}$$

where Q_{enc} represents the charge enclosed in the volume integral, this leads to

$$[\mathbf{D}]_\Gamma = \mathbf{n} \cdot [\epsilon \mathbf{E}]_\Gamma = q_s. \tag{2.24}$$

If we now apply Faraday's law to a thin rectangular loop traversing the interface, denoted by $\partial\Sigma$, which encloses an area Σ, i.e.,

$$\oint \mathbf{E} \cdot d\mathbf{l} = -\frac{d}{dt} \iint_\Sigma \mathbf{B} \cdot d\mathbf{S} = 0, \tag{2.25}$$

which due to the cancelling of the contributions from the circulation along the direction normal to the interface leaves us with

$$\mathbf{n} \times [\mathbf{E}]_\Sigma = 0. \tag{2.26}$$

The irrotational condition found in Eq. 2.26 ultimately means that the electric potential ϕ and the tangential electric fields $\mathbf{E}_{t_i}$ do not experience a jump through the interface.

$$[\phi]_\Gamma = 0, \tag{2.27}$$

$$[\mathbf{E}_{t_i}]_\Gamma = 0. \tag{2.28}$$

Stress Continuity

The assumption that the derivative of the velocity field is continuous leads us to conclude that the stress balance from the momentum equation has to be satisfied in the tangential and the normal direction, which gives us

$$\left[\mathbf{n}^\mathsf{T} \cdot \boldsymbol{\tau}\right]_\Gamma = \mathbf{f}_S, \tag{2.29}$$

where $\mathbf{f}_S$ represents the surface tension force acting on the interface. We will assume the surface tension coefficient γ to be the same all along the fluid interface, which leads to $\mathbf{f}_S = -\gamma\kappa\mathbf{n}$ where κ represents the curvature of the interface. If we project this condition into the tangential component of the coordinate system that we have defined, we arrive at:

$$\left[\mathbf{n}^\mathsf{T} \cdot (\boldsymbol{\sigma}^{ehd} + \boldsymbol{\sigma}) \cdot \mathbf{t}_i\right]_\Gamma = \left[\mathbf{n}^\mathsf{T} \cdot \boldsymbol{\sigma} \cdot \mathbf{t}_i\right]_\Gamma + q_S \mathbf{E} \cdot \mathbf{t}_i = 0. \tag{2.30}$$

Regarding the projection into the normal direction,

$$-\left[p\right]_\Gamma + \left[\mathbf{n}^\mathsf{T} \cdot (\boldsymbol{\sigma}^{ehd} + \boldsymbol{\sigma}) \cdot \mathbf{n}\right]_\Gamma = -\gamma\kappa. \tag{2.31}$$

It should be noted that Eqs. 2.22 and 2.21 mean that there has to be continuity in the tangential velocity gradients, which means that $\left[\mathbf{t}_i^\mathsf{T} \cdot \nabla\mathbf{u}\right]_\Gamma = 0$. Invoking the continuity equation $\nabla \cdot \mathbf{u}_\alpha = \mathbf{n}^\mathsf{T} \cdot \nabla\mathbf{u}_\alpha \cdot \mathbf{n} + \mathbf{t}_i^\mathsf{T} \cdot \nabla\mathbf{u}_\alpha \cdot \mathbf{t}_i = 0$, we can conclude that the normal component of the normal velocity gradient is continuous, that is

$$\left[\mathbf{n}^\mathsf{T} \cdot \nabla\mathbf{u} \cdot \mathbf{n}\right]_\Gamma = 0. \tag{2.32}$$

This allows us to write the viscous stress tensor jump in the following way:

$$\left[\mathbf{n}^\mathsf{T} \cdot \boldsymbol{\sigma} \cdot \mathbf{n}\right] = \left[\mathbf{n}^\mathsf{T} \cdot \mu\left(\nabla\mathbf{u} + \nabla\mathbf{u}^\mathsf{T}\right) \cdot \mathbf{n}\right]_\Gamma = 2\left[\mu\right]_\Gamma \mathbf{n}^\mathsf{T} \cdot \nabla\mathbf{u} \cdot \mathbf{n}. \tag{2.33}$$

Considering the contribution from the Maxwell stress tensor, we can write it as

$$\left[\mathbf{n}^\mathsf{T} \cdot \boldsymbol{\sigma}^{ehd} \cdot \mathbf{n}\right] = \frac{1}{2}\left[\epsilon\left(\mathbf{E} \cdot \mathbf{n}\right)^2 - \epsilon\left(\mathbf{E} \cdot \mathbf{t}_i\right)^2\right] = \frac{1}{2}\left[\epsilon\mathbf{E}_n^2\right] - \frac{1}{2}\left[\epsilon\mathbf{E}_{t_i}^2\right]. \tag{2.34}$$

Putting this all together into Eq. 2.31 we arrive at the following expression for the pressure jump at the interface:

$$\left[p\right]_\Gamma = 2\left[\mu\right]_\Gamma \mathbf{n}^\mathsf{T} \cdot \nabla\mathbf{u} \cdot \mathbf{n} + \gamma\kappa + \frac{1}{2}\left[\epsilon\mathbf{E}_n^2\right] - \frac{1}{2}\left[\epsilon\mathbf{E}_{t_i}^2\right]. \tag{2.35}$$

CHAPTER 3

CFD IMPLEMENTATION

3.1 General Aspects

In order to study EHD phenomena, NGA [24] was employed, an accurate and robust CFD code capable of performing Large Eddy Simulations (LES) and Direct Numerical Simulations (DNS) of liquid atomization, spray combustion, premixed and non-premixed turbulent combustion and particle laden flows. This code is formulated in high order fully conservative finite difference schemes, which provides high accuracy and excellent mass, momentum and energy conservation properties.

In order to accurately track the interface in multiphase flows, NGA uses an accurate level set method with a hyperbolic tangent, proposed by Desjardins et al. [25] [26], which allows it to have good conservation properties even with low mesh resolutions. The code is written with spatially staggered vector quantities, which are defined at cell faces instead of cell centres, allowing easy flux computation of quantities. This also allows it to have good accuracy with low order numerical schemes.

The solution procedure that will be employed makes use of a semi-implicit Crank-Nicholson scheme based in the time advancement scheme proposed by Pierce et al. [27], where the time advancement is staggered between the velocity field and the scalar and density fields. This scheme will be adapted, as was done in Tomar et al. [19] to deal with the electrohydrodynamic effects. The steps taken are as follows.

1. Advance the level set field for the interface from $t^{n-\frac{1}{2}}$ to $t^{n+\frac{1}{2}}$ with the velocity field at t^n.
2. Advance the velocity field from t^n to t^{n+1} by solving the incompressible Navier-Stokes equation using level set data from time $t^{n+\frac{1}{2}}$ without electrostatic effects or pressure terms.
3. Resolution of the Poisson equation for the pressure and for the electric potential ϕ.
4. Computation of the gradient of the potential, in order to find components of the electric field $\mathbf{E}$ at the cell faces.
5. Phase aware interpolation of the electric field to the cell center.
6. Calculation of the pressure jump at the interface due to the Maxwell stress tensor and surface tension.
7. Calculation of the pressure gradient and electrostatic force density in order to correct the velocity at t^{n+1}.

Regarding the interpolation of the electric field Cartesian components in the staggered configuration to the cell centres, the phase-aware algorithm developped by Van Poppel et al. [28] will be used.

In order to solve the systems of equations that will be encountered through this problem the Black-Box Multigrid (BBMG) solver of Dendy [29] will be used due to its robustness and efficiency.

3.2 Electric Potential Poisson Equation

The equation that we are ultimately trying to solve is

$$\nabla \cdot (\epsilon \nabla \phi) = -q, \tag{3.1}$$

Integrating over a volume and applying Gauss's theorem to the left hand side leads to

$$\oiint_{\Gamma} (\epsilon \nabla \phi)\, d\mathbf{S} = \iiint_{\Omega} -q dV, \tag{3.2}$$

where Ω refers to a given grid cell, and Γ to its boundary. This equation in 1D ultimately boils down to:

$$\left(\epsilon \frac{\partial \phi}{\partial x}\right)\Big|_{i+1/2} - \left(\epsilon \frac{\partial \phi}{\partial x}\right)\Big|_{i-1/2} = \int_{i-1/2}^{i+1/2} -q dx. \tag{3.3}$$

An important part of the flow solver is the crisp an accurate representation of the electric field and potential through the interface, which can be dealt with in the Finite Difference (FD) sense through the use of the Ghost Fluid Method, from the work of Fedkiw et al. [30, 31], which was applied to the electric potential Poisson equation by Van Poppel et al. [28], which explicitly includes the jump conditions stated earlier. This approach eliminates the problems that other strategies like the Continuum Surface Force (CSF) [32] face, the spreading of the jumps over the cells surrounding the interface, which Tomar et al. [19] employed to model the same phenomenon.

3.2.1 GFM implementation

Starting from Eq. 2.24, and assuming that there is no charge q_s at the interface, we are going to make the following assumption, first suggested by Liu et al. [31]:

$$[\epsilon \mathbf{E}]_{\Gamma} \approx [\epsilon E_n]_{\Gamma}\, \mathbf{n} = 0. \tag{3.4}$$

This assumption will avoid further problems down the road along the derivation, but it will lead to the false identity that $[\epsilon E_{t_i}]_\Gamma = 0$, which due to Eq. 2.28, we know that $[\epsilon E_{t_i}]_\Gamma = [\epsilon]_\Gamma E_{t_i}$. Despite the fact that we will only use Eq. 3.4 for the computation of the potential Poisson equation, it will only be valid if the jump in the tangential component is very small compared to the jump in the normal component. This hypothesis will ultimately allow us to reach a dimension-by-dimension scheme for the electric potential ϕ. If we rewrite Eq. 3.4 into its cartesian components

$$[\epsilon \mathbf{E}]_\Gamma = [\epsilon E_x]_\Gamma \mathbf{e}_x + \left[\epsilon E_y\right]_\Gamma \mathbf{e}_y + [\epsilon E_z]_\Gamma \mathbf{e}_z = 0, \tag{3.5}$$

we realize that each individual component of Eq. 3.5 must be equal to zero. Concentrating on $\mathbf{e}_x$, we can rewrite it as,

$$[\epsilon E_x]_\Gamma = [\epsilon]_\Gamma E_x^g + \epsilon_l [E_x]_\Gamma = 0, \tag{3.6}$$

$$[\epsilon E_x]_\Gamma = [\epsilon]_\Gamma E_x^l + \epsilon_g [E_x]_\Gamma = 0, \tag{3.7}$$

$$\tag{3.8}$$

which leads us to an interface jump along a given dimension of,

$$[E_x]_\Gamma = \frac{-[\epsilon]_\Gamma}{\epsilon_l} E_x^g = (1/\epsilon_r - 1) E_x^g, \tag{3.9}$$

$$[E_x]_\Gamma = \frac{-[\epsilon]_\Gamma}{\epsilon_g} E_x^l = (1 - \epsilon_r) E_x^l, \tag{3.10}$$

and similarly for $\left[E_y\right]_\Gamma$ and $[E_z]_\Gamma$ where $\epsilon_r = \epsilon_l/\epsilon_g$. Note that the Eqs. 3.9 and 3.10 represent dimension-by-dimension jump conditions for the electric field, with which we will be able to successfully discretize the electric potential Poisson equation. Consider the 1D schematic shown in Fig. 3.1.

We can Taylor expand ϕ at the interface Γ on each side, as follows:

$$[\phi]_i = [\phi]_\Gamma + (x_i - x_\Gamma) [\nabla_x \phi]_\Gamma + O\left((x_i - x_\Gamma)^2\right), \tag{3.11}$$

$$[\phi]_{i+1} = [\phi]_\Gamma + (x_{i+1} - x_\Gamma) [\nabla_x \phi]_\Gamma + O\left((x_{i+1} - x_\Gamma)^2\right), \tag{3.12}$$

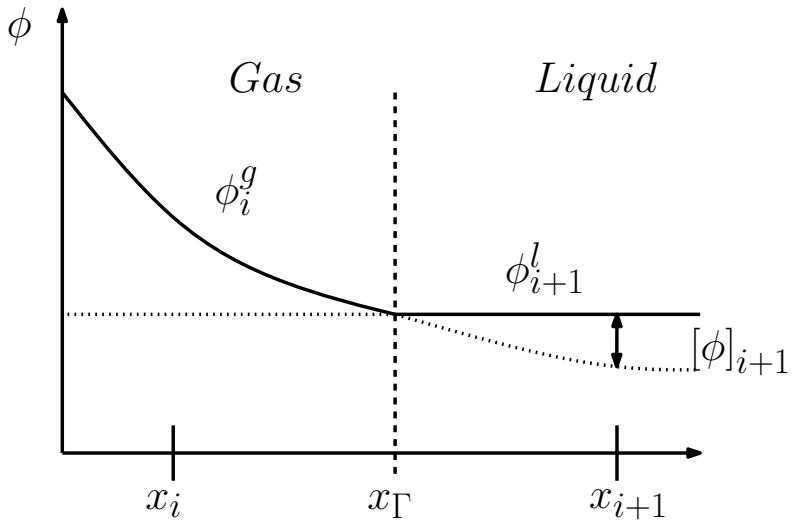

Figure 3.1: GFM Schematic.

and due to the fact that $[\phi]_\Gamma = 0$, and that Eqs. 3.9 and 3.10 provide an approximation of $[\nabla\phi]_\Gamma$, we can write,

$$[\phi]_i \approx -(x_i - x_\Gamma)\,[E_x]_\Gamma = -(x_i - x_\Gamma)\,\frac{[\epsilon]_\Gamma\, E_x^l|_\Gamma}{\epsilon_g}, \tag{3.13}$$

$$[\phi]_{i+1} \approx -(x_{i+1} - x_\Gamma)\,[E_x]_\Gamma = -(x_{i+1} - x_\Gamma)\,\frac{[\epsilon]_\Gamma\, E_x^g|_\Gamma}{\epsilon_l}. \tag{3.14}$$

Note that we are using the value of the electric field E_x corresponding to the fluid phase we are on. Approximating these derivatives we arrive at

$$E_x^l|_\Gamma \approx E_x^l|_{i+1/2} = \frac{\phi_{i+1}^l - \phi_i^l}{\triangle x} = \frac{\phi_{i+1}^l - \phi_i^g}{\triangle x} - \frac{[\phi]_i}{\triangle x}, \tag{3.15}$$

$$E_x^g|_\Gamma \approx E_x^g|_{i+1/2} = \frac{\phi_{i+1}^g - \phi_i^g}{\triangle x} = \frac{\phi_{i+1}^l - \phi_i^g}{\triangle x} - \frac{[\phi]_{i+1}}{\triangle x}. \tag{3.16}$$

Plugging Eq. 3.15 into Eq. 3.13 we arrive at

$$[\phi]_i \approx -(x_i - x_\Gamma)\,\frac{[\epsilon]_\Gamma}{\epsilon_g}\left(\frac{\phi_{i+1}^l - \phi_i^g}{\triangle x} - \frac{[\phi]_i}{\triangle x}\right). \tag{3.17}$$

Defining a liquid fraction index as $\theta = (x_{i+1} - x_\Gamma)/\triangle x$, the previous expression can be written as

$$[\phi]_i = \left(1 - \frac{\epsilon_g}{(1-\theta)\,\epsilon_l + \theta\epsilon_g}\right)\left(\phi_{i+1}^l - \phi_i^g\right). \tag{3.18}$$

Further defining $\epsilon^* = (1-\theta)\,\epsilon_l + \theta\epsilon_g$, allows us to calculate the gradient in the liquid or the gas phase as:

$$\left.\frac{\partial\phi}{\partial x}\right|^{l}_{i+1/2} = \frac{\epsilon_g}{\epsilon^*}\left(\frac{\phi^l_{i+1}-\phi^g_i}{\triangle x}\right), \tag{3.19}$$

$$\left.\frac{\partial\phi}{\partial x}\right|^{g}_{i+1/2} = \frac{\epsilon_l}{\epsilon^*}\left(\frac{\phi^g_{i+1}-\phi^l_i}{\triangle x}\right). \tag{3.20}$$

3.2.2 Finite Volume Implementation

The boundary conditions we are facing allow for a natural Finite Volume treatment of the problem, consider the following interface configuration, where we have assumed that out potential ϕ is linear, as depicted in Fig. 3.2.

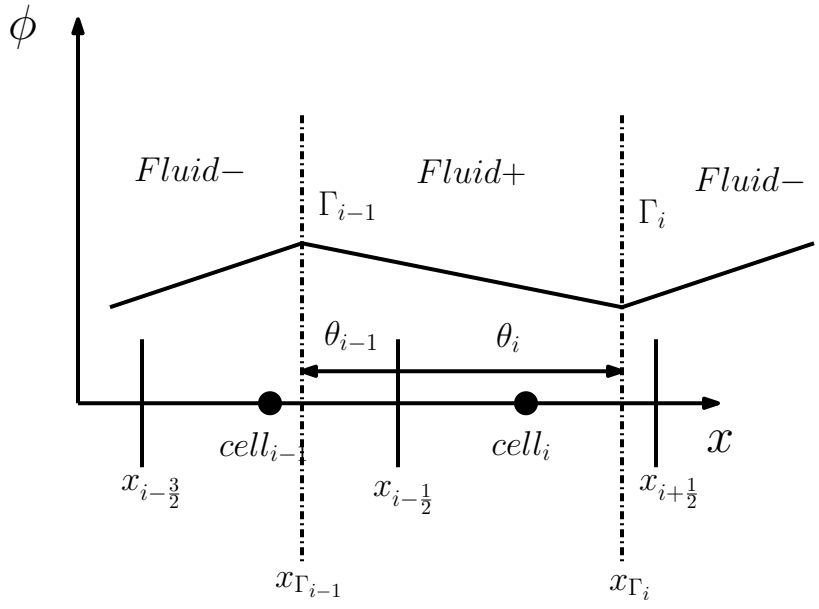

Figure 3.2: Finite Volume Schematic.

The schematic shows two adjacent cells, on which two consecutive jumps can be seen (comments will be made later on regarding the number of jumps that we can accurately simulate). Fluid "+" has electrical permittivity ϵ_+,

while fluid "-" has electrical permittivity ϵ_+. The variable θ_i represents the quantity of fluid "+" that is in a given cell. If we consider the profile of ϕ_+ as linear, we can assume that,

$$\epsilon_- \frac{\partial \phi}{\partial x}\bigg|_{\Gamma_i^-} = \epsilon_+ \frac{\partial \phi}{\partial x}\bigg|_{\Gamma_i^+} = \epsilon_- \frac{\partial \phi}{\partial x}\bigg|_{\Gamma_{i-1}^-}. \tag{3.21}$$

This means that we will assume that $\frac{\partial \phi}{\partial x}\big|_{\Gamma_{i-1}^-} = \frac{\partial \phi}{\partial x}\big|_{\Gamma_i^-}$. From now onwards we will drop the i index in the derivatives, and we will use $\frac{\partial \phi}{\partial x}\big|_{\Gamma^-}$ and $\frac{\partial \phi}{\partial x}\big|_{\Gamma^+}$ Consider now a Taylor expansion around the interface Γ_i,

$$\phi_+^i(x) = \phi_+^{i-1}(x) = \phi_{\Gamma_i^+} + (x - x_\Gamma) \frac{\partial \phi}{\partial x}\bigg|_{\Gamma_i^+}, \tag{3.22}$$

$$\phi_-^i(x) = \phi_{\Gamma_i^-} + (x - x_\Gamma) \frac{\partial \phi}{\partial x}\bigg|_{\Gamma_i^-}. \tag{3.23}$$

In the previous expressions, ϕ_+^i and ϕ_+^{i-1} represent approximations in fluid "+", and ϕ_-^i represents an approximation in fluid "-" at cell i. Our boundary conditions imply that $[\phi] = \phi_{\Gamma_i^+} - \phi_{\Gamma_i^-} = 0$. From now onwards, we will denote the values of ϕ at Γ_i as ϕ_{Γ_i} We can extend our Taylor expansion to the "-" fluid in cell $i-1$ by taking into account that,

$$\phi_{\Gamma_{i-1}} = \phi_{\Gamma_i} - (\theta_{i-1} + \theta_i) \triangle x \frac{\partial \phi}{\partial x}\bigg|_{\Gamma^+}, \tag{3.24}$$

where $\triangle x$ represents the dimension along the x direction of the homogeneous stencil that we are considering. Taylor expanding around Γ_{i-1} to find $\phi_-^{i-1}(x)$ gives

$$\phi_-^{i-1}(x) = \phi_{\Gamma_i} - (\theta_i + \theta_{i-1}) \triangle x \frac{\partial \phi}{\partial x}\bigg|_{\Gamma^+} + (x - (x_{\Gamma_i} - (\theta_i + \theta_{i-1}))) \frac{\partial \phi}{\partial x}\bigg|_{\Gamma^-}. \tag{3.25}$$

As we can see we have been able to find expressions for $\phi(x)$ in terms of two parameters that we have knowledge of at the cell center; θ_i and θ_{i-1} and three variables of which we have no knowledge; $\frac{\partial \phi}{\partial x}\big|_{\Gamma^-}$, $\frac{\partial \phi}{\partial x}\big|_{\Gamma^+}$ and ϕ_{Γ_i}.

If we integrate over cell $i-1$ and divide by the size of the cell $\triangle x$, we will arrive at the following volume averaged quantity:

$$\frac{1}{\triangle x}\int_{i-\frac{3}{2}}^{i-\frac{1}{2}} \phi^{i-1}(x)\,dx = \overline{\phi}_{i-1}. \tag{3.26}$$

Plugging the Taylor expansions found in Eqs. 3.22 and 3.25 and integrating over cell $i-1$ we reach

$$\begin{aligned}
\triangle x\overline{\phi}_{i-1} &= \int_{i-\frac{3}{2}}^{\Gamma_{i-1}} \phi_-^{i-1}dx + \int_{\Gamma_{i-1}}^{i-\frac{1}{2}} \phi_+^{i-1}dx \\
&+ \int_{i-\frac{3}{2}}^{\Gamma_{i-1}} \left(\phi_{\Gamma_i} - (\theta_i+\theta_{i-1})\triangle x\frac{\partial\phi}{\partial x}\Big|_{\Gamma^+}\right)dx \\
&+ \int_{i-\frac{3}{2}}^{\Gamma_{i-1}} \left(x - x_{\Gamma_i} + (\theta_i+\theta_{i-1})\triangle x\frac{\partial\phi}{\partial x}\Big|_{\Gamma^-}\right)dx \\
&+ \int_{\Gamma_{i-1}}^{i-\frac{1}{2}} \left(\phi_\Gamma - (x-x_{\Gamma_i})\frac{\partial\phi}{\partial x}\Big|_{\Gamma^+}\right)dx.
\end{aligned} \tag{3.27}$$

This leads to,

$$\begin{aligned}
\triangle x\overline{\phi}_{i-1} &= \phi_{\Gamma_i}\triangle x - (1-\theta_{i-1})\triangle x^2(\theta_i+\theta_{i-1})\frac{\partial\phi}{\partial x}\Big|_{\Gamma^+} \\
&+ \frac{1}{2}\frac{\partial\phi}{\partial x}\Big|_{\Gamma^-}(1-\theta_{i-1})^2\triangle x^2 \\
&+ \frac{1}{2}\frac{\partial\phi}{\partial x}\Big|_{\Gamma^+}\left(\theta_i^2 - (\theta_i+\theta_{i-1})^2\right)\triangle x^2.
\end{aligned} \tag{3.28}$$

If we apply the same procedure to cell i we reach.

$$\triangle x\overline{\phi}_i = \phi_{\Gamma_i}\triangle x - \frac{1}{2}\frac{\partial\phi}{\partial x}\Big|_{\Gamma^+}\theta_i^2\triangle x^2 + \frac{1}{2}\frac{\partial\phi}{\partial x}\Big|_{\Gamma^-}(1-\theta_i)^2\triangle x^2. \tag{3.29}$$

If we now take Eq. 3.29 minus Eq. 3.28 and we divide by $\triangle x^2$ we arrive at the following expression:

$$\begin{aligned}
\frac{\overline{\phi}_i - \overline{\phi}_{i-1}}{\triangle x} &= \frac{1}{2}\frac{\partial\phi}{\partial x}\Big|_{\Gamma^-}\left((1-\theta_i)^2 - (1-\theta_{i-1})^2\right) \\
&+ \frac{1}{2}\frac{\partial\phi}{\partial x}\Big|_{\Gamma^+}\left(-\theta_i^2 - \theta_{i-1}^2 + 2(\theta_i+\theta_{i-1})\right).
\end{aligned} \tag{3.30}$$

Remembering the interface condition given by Eq. 2.24, which states that $\epsilon_+\frac{\partial\phi}{\partial x}\Big|_{\Gamma_+} = \epsilon_-\frac{\partial\phi}{\partial x}\Big|_{\Gamma_-}$, we are able to write an expression for the derivative, be it in the

"+" or "-" fluid, i.e.,

$$\left.\frac{\partial \phi}{\partial x}\right|_{\Gamma^+} = \frac{\overline{\phi}_i - \overline{\phi}_{i-1}}{\triangle x} \frac{1}{f_+\left(\theta_i, \theta_{i-1}, \epsilon_r\right)}, \tag{3.31}$$

$$\left.\frac{\partial \phi}{\partial x}\right|_{\Gamma^-} = \frac{\overline{\phi}_i - \overline{\phi}_{i-1}}{\triangle x} \frac{1}{f_-\left(\theta_i, \theta_{i-1}, \epsilon_r\right)}, \tag{3.32}$$

where the functions $f_+ = f_+\left(\theta_i, \theta_{i-1}, \epsilon_r\right)$ and $f_- = f_-\left(\theta_i, \theta_{i-1}, \epsilon_r\right)$ are

$$f_+ = \frac{1}{2}\left(-\theta_i^2 - \theta_{i-1}^2 + 2\left(\theta_i + \theta_{i-1}\right) + \frac{\epsilon_+}{\epsilon_-}\left((1-\theta_i)^2 + (1-\theta_{i-1})^2\right)\right), \tag{3.33}$$

$$f_- = \frac{1}{2}\left(-\theta_i^2 - \theta_{i-1}^2 + 2\left(\theta_i + \theta_{i-1}\right) + \frac{\epsilon_-}{\epsilon_+}\left((1-\theta_i)^2 + (1-\theta_{i-1})^2\right)\right). \tag{3.34}$$

It should be noted that for the case we are considering, with a linear assumption, the derivative that we are interested in lies between cell i and $i-1$, where $x = x_{i-\frac{1}{2}}$, and therefore with the scheme that we have built we arrive at,

$$\left.\frac{\partial \phi}{\partial x}\right|_{\Gamma^+} = \left.\frac{\partial \phi}{\partial x}\right|_{x=x_{i-\frac{1}{2}}} = \frac{\overline{\phi}_i - \overline{\phi}_{i-1}}{\triangle x} \frac{1}{f_+\left(\theta_i, \theta_{i-1}, \epsilon_r\right)}. \tag{3.35}$$

This expression will be valid for all cell faces, regardless of if there is an interface between cell i and cell $i-1$. If we take for example two consecutive cells without an interface, we will verify that $\theta_i = 1$ and $\theta_{i-1} = 1$, which if we plug into Eq. 3.35 will give us the following derivative at the interface,

$$\left.\frac{\partial \phi}{\partial x}\right|_{x=x_{i-\frac{1}{2}}} = \frac{\overline{\phi}_i - \overline{\phi}_{i-1}}{\triangle x} \frac{1}{f_+\left(\theta_i = 1, \theta_{i-1} = 1, \epsilon_r\right)} = \frac{\overline{\phi}_i - \overline{\phi}_{i-1}}{\triangle x}, \tag{3.36}$$

which is simply the central difference formula. This formula is also valid for the cases where either $\theta_i = 1$ or $\theta_{i-1} = 1$. The schematic depicted in Fig. 3.2 where we have two interfaces at two contiguous cells was simply an artifice to arrive at an expression that would give us correct values for the derivative regardless of if we had a single interface at cell i or at cell $i-1$. This will be the case from now onwards, as none of the simulations that we will be considering will have two interfaces in two adjacent cells.

If instead of having fluid "+" at the cell face, we had fluid "-" at the face as can be seen in Fig. 3.3, the same expressions would be valid, but now $\theta_i = \theta_i^-$ and $\theta_{i-1} = \theta_{i-1}^-$ represent the volume of fluid "-" contained in cells i and $i-1$ respectively, and we would have to use f_- instead of f_+ for the calculation of the derivative. Thus the expressions would yield,

$$\left.\frac{\partial \phi}{\partial x}\right|_{\Gamma^-} = \left.\frac{\partial \phi}{\partial x}\right|_{x=x_{i-\frac{1}{2}}} = \frac{\overline{\phi}_i - \overline{\phi}_{i-1}}{\triangle x} \frac{1}{f_-\left(\theta_i^-, \theta_{i-1}^-, \epsilon_r\right)}. \tag{3.37}$$

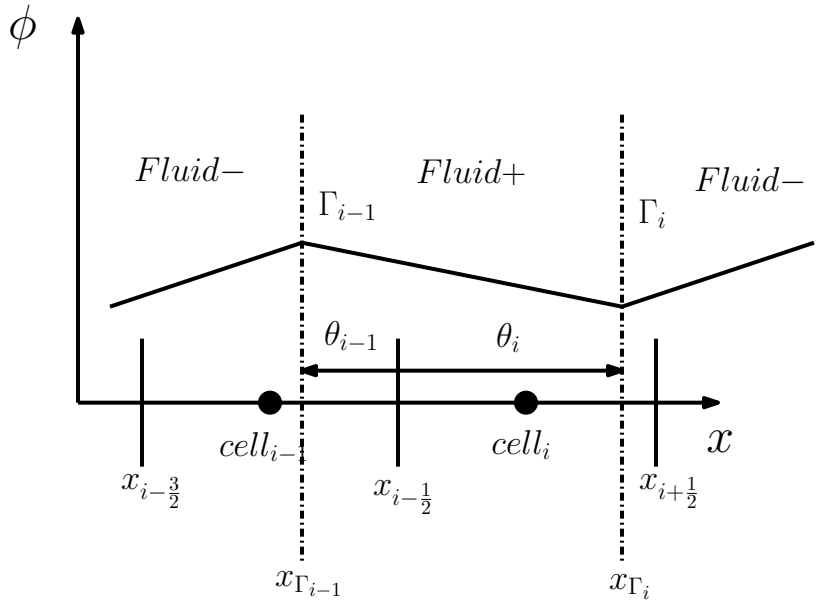

Figure 3.3: Finite Volume Schematic with fluid "-" at the cell face.

3.2.3 Continuum Surface Force Implementation

As was mentioned earlier, the Continuum Surface Force approach aims at smearing out transport and thermodynamic properties in the normal direction in a transition region of size, 2δ adjacent to the interface. This was first used to model the pressure jump caused by surface tension by Brackbill et al. [32], and

later extended to also deal with the pressure jump caused by electric effects by Tomar et al. [19]. This would result in a volumetric force exerted in the vicinity of the interface, instead of a surface force felt at the interface, as schematically depicted in Fig. 3.4.

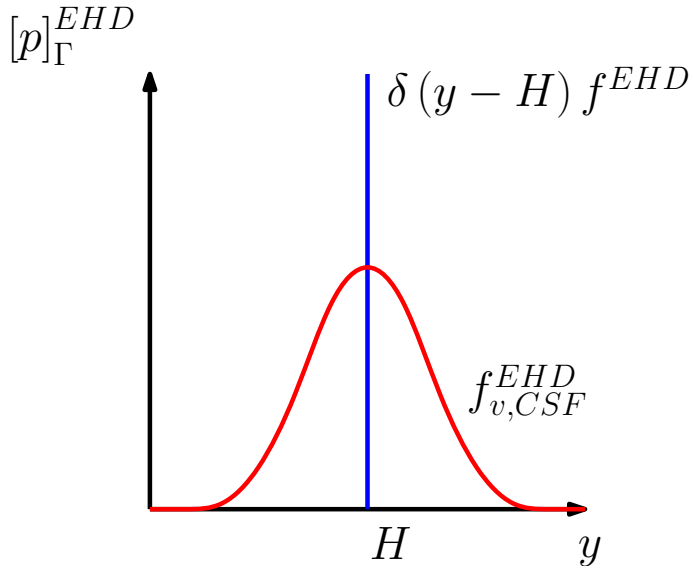

Figure 3.4: GFM and FV vs. CSF representation of EHD effects.

In order for this scheme to be mathematically sound, the following properties have to be verified:

1. The volumetric force integrated along the normal direction to the interface must be equal to the surface force.
2. As the width of the transition region goes to zero ($2\delta \to 0$), the volumetric force must reduce to the surface force.

The force defined in Eq. 2.8 verifies the Condition 1, but does not verify Condition 2, due to the the fact that the normal electric field E_t has a jump at the interface. Following Brackbill's [32] and Tomar's [19] methodology. Taking into

account that we are considering dielectric liquids, such that $q = 0$, with permittivities that are constant in each fluid, and expanding the electric field $\mathbf{E}$ into normal and tangential components, the surface force reduces to the following expression for the dielectric force

$$\mathbf{f}^{EHD} = \frac{1}{2}\left(-\left(\mathbf{E}\cdot\mathbf{n}\right)^2\nabla\epsilon - \left(\mathbf{E}\cdot\mathbf{t}\right)^2\nabla\epsilon\right). \tag{3.38}$$

Multiplying and dividing Eq. 3.38 by ϵ we arrive at

$$\mathbf{f}^{EHD} = \frac{1}{2}\left(\left(\epsilon\mathbf{E}\cdot\mathbf{n}\right)^2\nabla\left(\frac{1}{\epsilon}\right) - \left(\mathbf{E}\cdot\mathbf{t}\right)^2\nabla\epsilon\right). \tag{3.39}$$

Due to Eqs. 2.24 and 2.28 we know that the quantities in the formula are continuous in a medium where ϵ varies with space, and thus we can see that the volume force also verifies Condition 2, and the surface force f^{EHD} to which it reduces to, as found in Tomar et al. [19], is

$$\mathbf{f}^{EHD} = \frac{1}{2}\left(\left(\mathbf{D}\cdot\mathbf{n}\right)^2\left(\frac{1}{\epsilon_l} - \frac{1}{\epsilon_g}\right) - \left(\mathbf{E}\cdot\mathbf{t}\right)^2\left(\epsilon_l - \epsilon_g\right)\right)\mathbf{n}\delta_s, \tag{3.40}$$

where δ_s is the surface Dirac-delta function. Note that as Tomar et al. [19] pointed out Eq. 3.40 is obtained from Eq. 2.34 by considering that $\nabla\epsilon \rightarrow \|\epsilon\|\mathbf{n}\delta_s$ and that $\nabla\left(\frac{1}{\epsilon}\right) \rightarrow \|\frac{1}{\epsilon}\|\mathbf{n}\delta_s$ as $2\delta \rightarrow 0$.

CSF Numerical Implementation

In order to be able to solve the electric potential Poisson Eq. 3.1 consistently with this approach, the electrical properties need to be smeared out with an indicator function $\mathcal{I}$ in the transition region between the two fluids. This transition function will have a value of unity in the liquid and zero in the gas, and will vary smoothly in the vicinity of the interface along the normal direction. As Tomar et al. [19] demonstrated, the use of a weighted harmonic mean (WHM)

interpolation scheme, such as the one found in Eq. 3.41 yields better results than a weighted arithmetic mean interpolation (WAM).

$$\frac{1}{\epsilon} = \frac{\mathcal{I}}{\epsilon_l} + \frac{\mathcal{I} - 1}{\epsilon_g}. \tag{3.41}$$

The indicator function $\mathcal{I}$ that will be used will be the hyperbolic tangent level set function described by Olsson and Kreiss [33] and Olsson et al. [34], instead of the piecewise function found in Tomar et al. [19]. The hyperbolic function will be transported and re-initialized using conservative equations, and can be found in Eq. 3.42. This level set function was used by Desjardins et al. [25] to simulate turbulent atomization in 2008.

$$\psi(\mathbf{x}, t) = \frac{1}{2}\left(\tanh\left(\frac{\Phi(\mathbf{x}, t)}{2\delta}\right) + 1\right), \tag{3.42}$$

where $\Phi(\mathbf{x}, t)$ represents the signed distance level set function that verifies that $\Phi(\mathbf{x}, t) > 0$ on one side of the interface and $\Phi(\mathbf{x}, t) < 0$ on the other.

The electric volumetric force for dielectric fluids $f_{v,CSF}^{EHD}$, which we have already shown to be equivalent to the electric field surface force, is given in Eq.3.43

$$f_{v,CSF}^{EHD} = \frac{1}{2}\left(\frac{(\epsilon\mathbf{E}\cdot\mathbf{n})^2}{\epsilon_l\epsilon_g} + (\mathbf{E}\cdot\mathbf{t})^2\right)\left(\epsilon_l - \epsilon_g\right)\nabla\mathcal{I}. \tag{3.43}$$

In the numerical scheme employed in this methodology, the Laplacian of the potential Poisson equation, found in Eq. 3.1, is discretized by evaluating the product of the derivative of the potential times the smeared our permittivity at the cell faces surrounding the volume. In order to move the values of the permittivity ϵ from the cell centres to the faces, we take the inverse of the linear interpolation of the inverse of the permittivity at the cell centres, arriving at a harmonic average at the face.

Once the values of the potential ϕ are found at the cell centres, a central difference scheme is employed to compute the value of the components of the

electric field at the cell faces. These values are used in a corrector step, which integrates the body force in the vicinity of the interface, where $\nabla \mathcal{I}$ is non-zero. As Tomar et al. [19] note, the use of WHM in evaluating the term $(\mathbf{E} \cdot \mathbf{t})^2 \nabla \epsilon$ results in a function that leads to inaccuracies in the jump accross the interface, and so the expression $(\mathbf{E} \cdot \mathbf{t})^2 \left(\epsilon_l - \epsilon_g\right) \nabla \mathcal{I}$ in Eq. 3.43 is used instead.

CHAPTER 4

VALIDATION

Several analytical test cases will be studied in order to determine the accuracy of the different available tools for solving the electric potential Poisson equation.

4.1 1D Study

4.1.1 Horizontal Liquid-Gas Interface

The first analytical problem that will be studied will be that of a 1D interface between two fluids, in the configuration shown in the next image. Note that for this 1D problem, the harmonic averaging of the Laplacian coefficients and the GFM method are identically equivalent. The gaseous domain, with permittivity

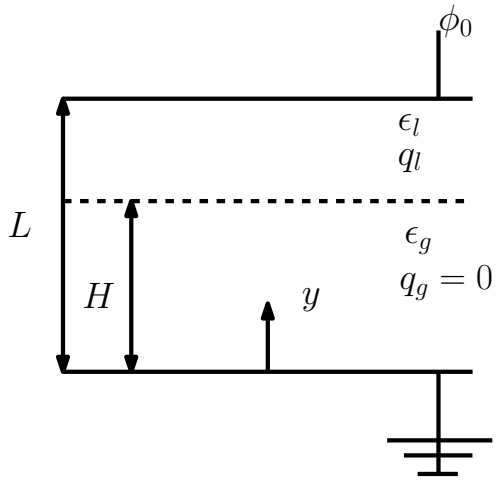

Figure 4.1: Horizontal interface with charge density.

ϵ_g extends from $0 \leq y < H$, whereas the liquid domain, with permittivity ϵ_l

extends from $H \leq y \leq 1$. It should be noted that the charge density of the gas is $q_g = 0$ C/m, whereas the charge density $q_l \neq 0$. The analytical solution for this case gives an electric field $\mathbf{E}^l$ and $\mathbf{E}^g$,

$$E^l(y) = \frac{q_l y}{\epsilon_l} - \beta \quad \text{for} \quad 0 \leq y < H, \tag{4.1}$$

$$E^g(y) = \epsilon_r \left(\frac{q_g H}{\epsilon_l} - \beta \right) \quad \text{for} \quad H \leq y \leq 1, \tag{4.2}$$

where the parameter β equals,

$$\beta = \frac{\epsilon_g q_l \left(L^2 - H^2 \right) / (2\epsilon_l) + H^2 q_l + \epsilon_g \phi_0}{\epsilon_g (L - H) + H\epsilon_l}. \tag{4.3}$$

The simulation was performed for $L = 1$ m, $H = 0.4$ m, $\epsilon_l = 5$ F/m, $\epsilon_g = 1$ F/m, $\phi = 100$ V and $q_l = \phi/(L - H)$ C/m. All three implementations give a crisp representation of the electric field, even with very coarse meshes, in contrast to the weighed harmonic mean transition region scheme, implemented by Tomar et al. [19] using a coupled level set and volume-of fluid (CLSVOF) approach, which smears out the jump over several points, as can be seen in the image of the normalized electric field, shown in Fig. 4.3, where the CSF approach was used with $2\delta = L/3$.

As was mentioned earlier, the CSF methodology would give rise to a volumetric EHD force felt in the regions of the domain where $\nabla \mathcal{I}$ is non-zero.

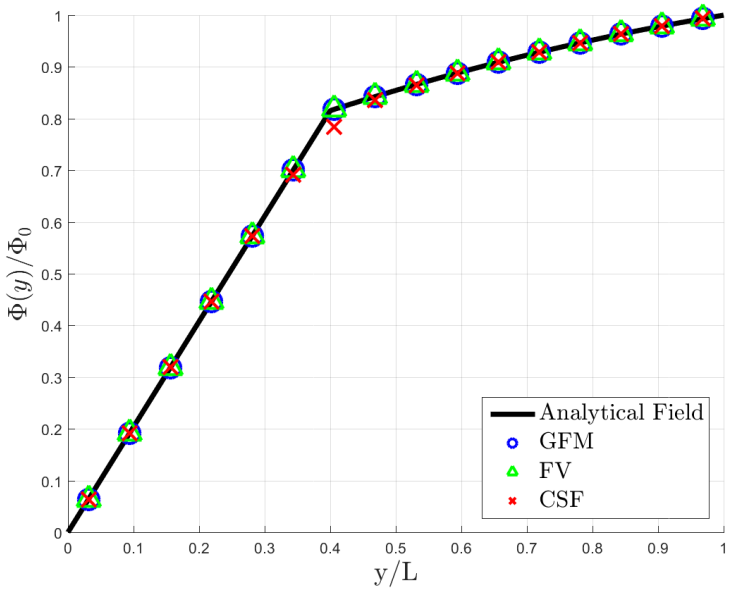

Figure 4.2: ϕ/ϕ_0 as a function of y for the horizontal flat interface.

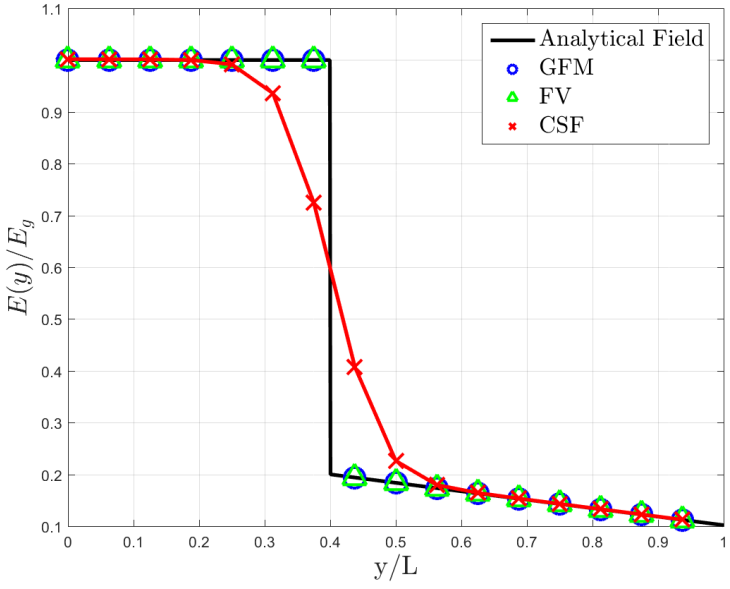

Figure 4.3: E_y/E_g as a function of y for the horizontal flat interface.

The normalized errors computed in E_y and ϕ in the L_2, L_1 and L_∞ norm are shown next in Figs. 4.4,4.5, 4.6, 4.7, 4.8 and 4.9 for the jump-preserving methods. It should be noted that both the pure GFM, and the harmonic and arithmetic weighting of the coefficients are compared to the analytical solution in the point-wise sense for the potential ϕ, while the new FV scheme is compared to the volume averaged analytical solution. As was mentioned earlier, the GFM and the Harmonic averaging approach are equivalent in this simple 1D case, and thus both of these lines are indistinguishable in the following plots.

The errors for ϕ and $\mathbf{E}$ are not shown for the CSF approach, due to the fact that this method aims at spreading out the jump in the electric field over the transition region. It would thus have a much greater errors in calculating the electric field than any of the jump preserving methods, despite the fact that as will be shown later on, it performs well in calculating the pressure jump $[p]_\Gamma$.

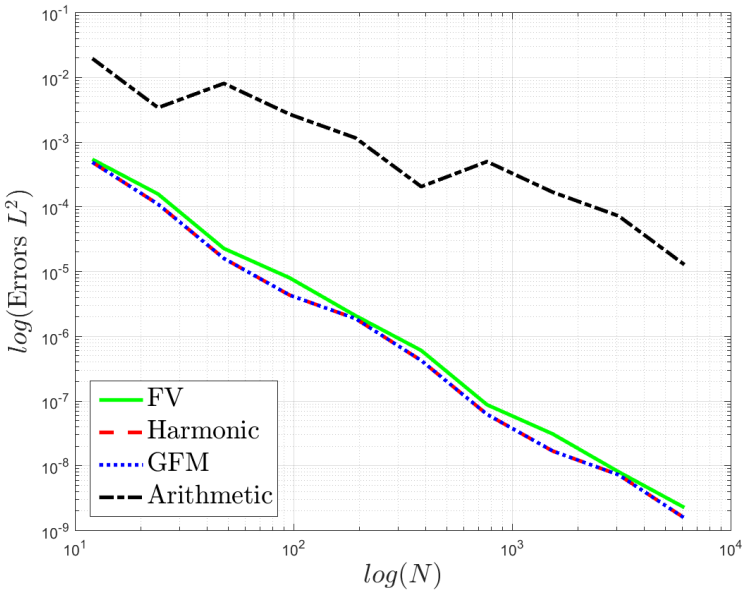

Figure 4.4: Error in the L^2 norm for the horizontal interface potential.

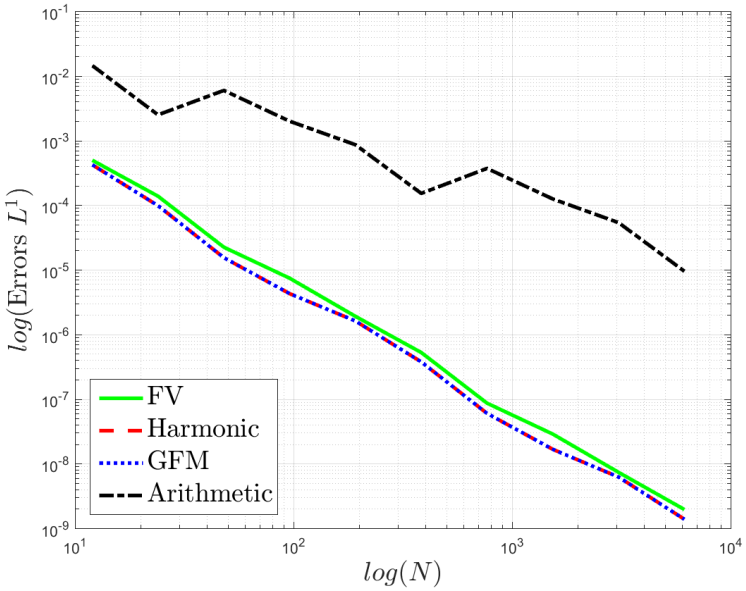

Figure 4.5: Normalized error in the L^1 norm for the horizontal interface potential.

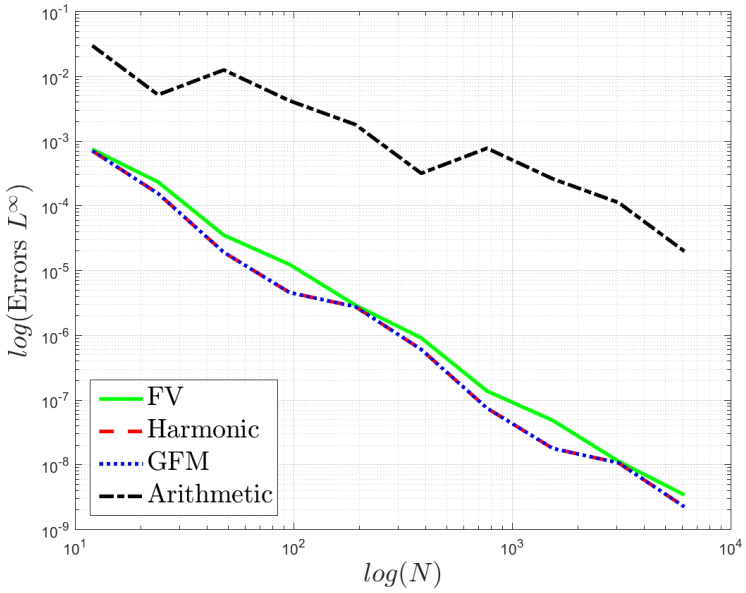

Figure 4.6: Normalized error in the L^∞ norm for the horizontal potential.

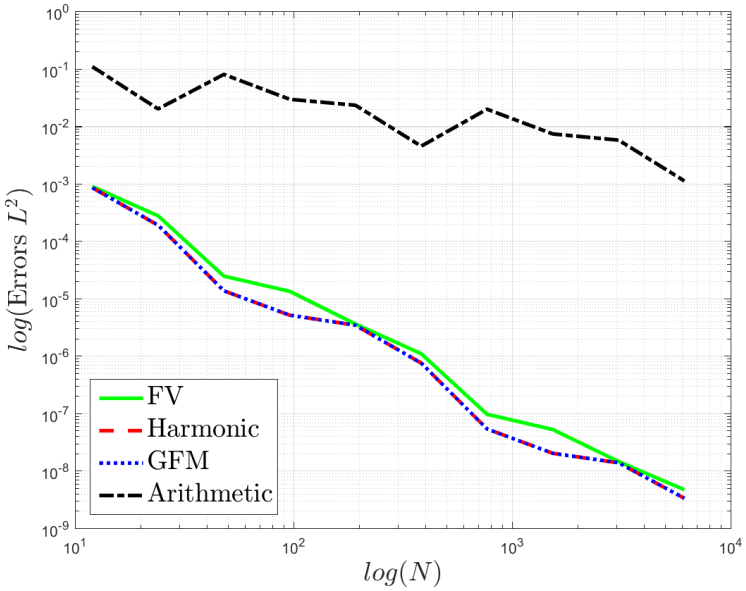

Figure 4.7: Normalized error in the L^2 norm for the horizontal interface electric field.

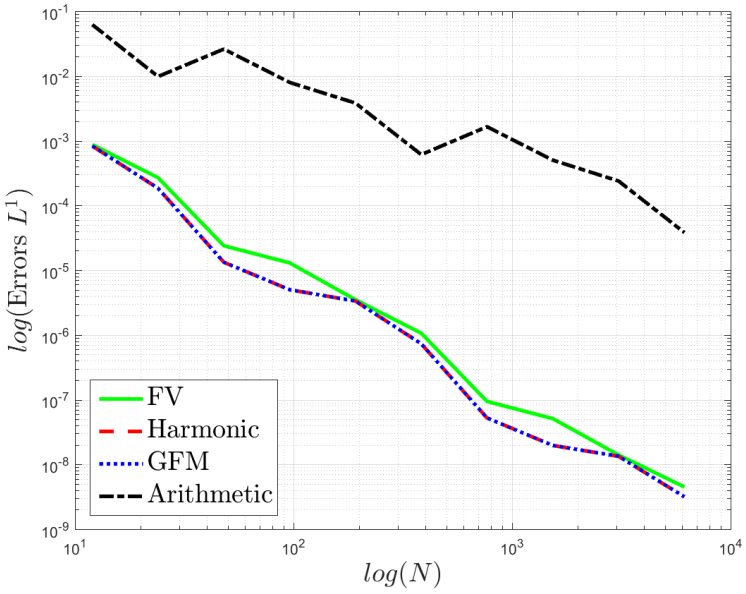

Figure 4.8: Normalized error in the L^1 norm for the horizontal interface electric field.

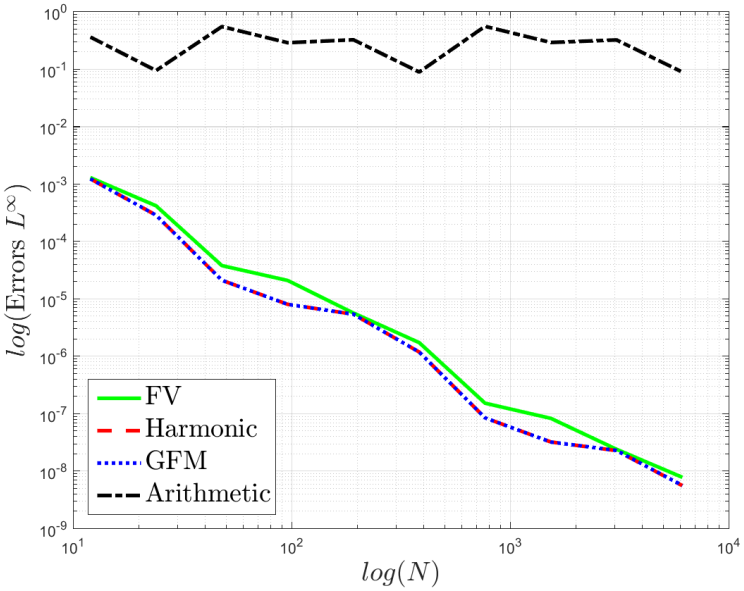

Figure 4.9: Normalized error in the L^∞ norm for the horizontal interface electric field.

The error in the pressure jump can be found in Table 4.1 for the four different methods that were implemented, where CPR denotes cells per radius, equivalent to R/h, where h is the grid spacing. When comparing to the results of Tomar et al. [19], it should be noted that they do not consider a non-zero charge density in the liquid, as is done in the present work. The Finite Volume (FV) scheme presents a $8.716 \cdot 10^{-3}$ % error for 8 points across the domain if no charge is present in the system, comparable to the results reported in Tomar et al. [19] for 40 points in the domain.

As we can see, the new finite volume scheme has an accuracy comparable to the harmonic averaging of the permittivity in the Laplacian, and the GFM scheme in all norms, both for the electric potential and field. On the other hand, the simplest of our schemes, arithmetic averaging of the permittivity performs

	Method			
CPR	GFM	FV	HA	AA
8	4.79	4.85	4.79	98.56
16	0.63	0.68	0.63	50.88
32	0.29	0.28	0.286	24.05

Table 4.1: Error (%) in the calculation of the pressure jump $[p]$ at the interface.

poorly in comparison.

From now onwards, we will concentrate in the new Finite Volume (FV) scheme, the harmonic averaging of the permittivity and the GFM method in our validation. These schemes have shown second order accuracy in all norms for the potential and the electric field for this simple 1D case.

4.2 2D Study

In this section, we will study the error behaviour when the 1D scheme is applied to 2D problems, with non mesh-aligned curved interfaces.

4.2.1 Method of Manufactured Solutions (MMS)

We will use the Method of Manufactured Solutions (MMS) to arrive at a RHS for Eq. 3.1, that also verifies the conditions found in Eqs. 2.24, 2.27 and 2.28 at the interface.

Considering a 2D square domain with a liquid disc immersed in gas, as can be seen in Fig. 4.10, the solution that was tested was given by,

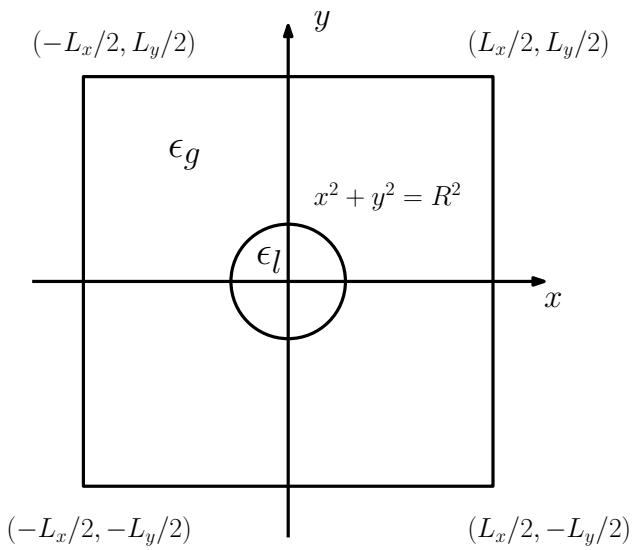

Figure 4.10: MMS geometry for 2D Validation.

$$\phi^l(x,y) = \left(x^2 + y^2 - R^2\right) \cos\frac{2\pi x}{L_x} \cos\frac{2\pi y}{L_y} \text{ V} \quad \text{for} \quad x^2 + y^2 < R^2, \tag{4.4}$$

$$\phi^g(x,y) = 2\left(x^2 + y^2 - R^2\right) \cos\frac{2\pi x}{L_x} \cos\frac{2\pi y}{L_y} \text{ V} \quad \text{for} \quad x^2 + y^2 \geq R^2, \tag{4.5}$$

where for our test case $R = 0.2m$, $\epsilon_g = 2$ F/m, $\epsilon_l = 1$ F/m and $L_x = L_y = 1$ m. The evolution of the error in ϕ is shown in Figs. 4.11, 4.12 and 4.13, while the evolution of $\mathbf{E} \cdot \mathbf{e}_y = E_y$ is shown in figures 4.14, 4.15 and 4.16. Due to the smeared out nature of the CSF approach, no error analysis was made for the potential and the electric field in this MMS case. A comparison between the errors in the pressure jump $[p]_\Gamma$ for the CSF and the jump preserving methods can be found in the end of Section 4.2.2.

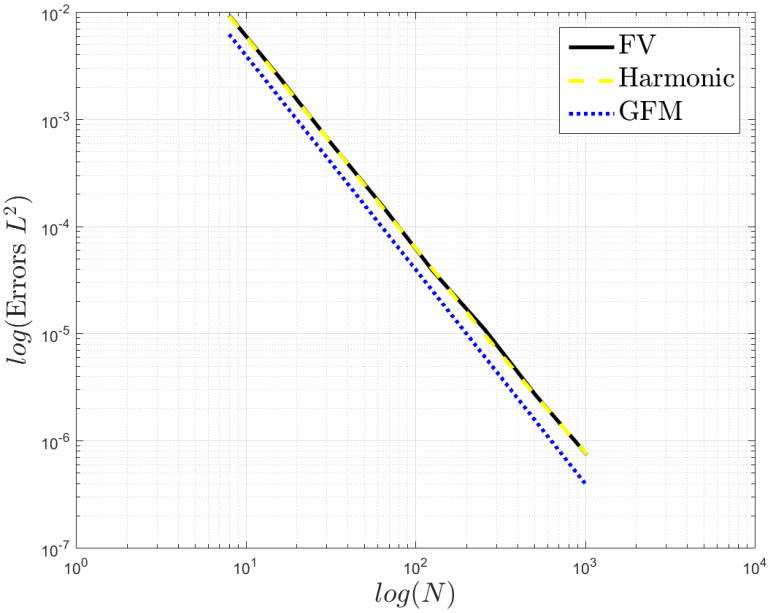

Figure 4.11: ϕ error in the L^2 norm for the 2D MMS validation.

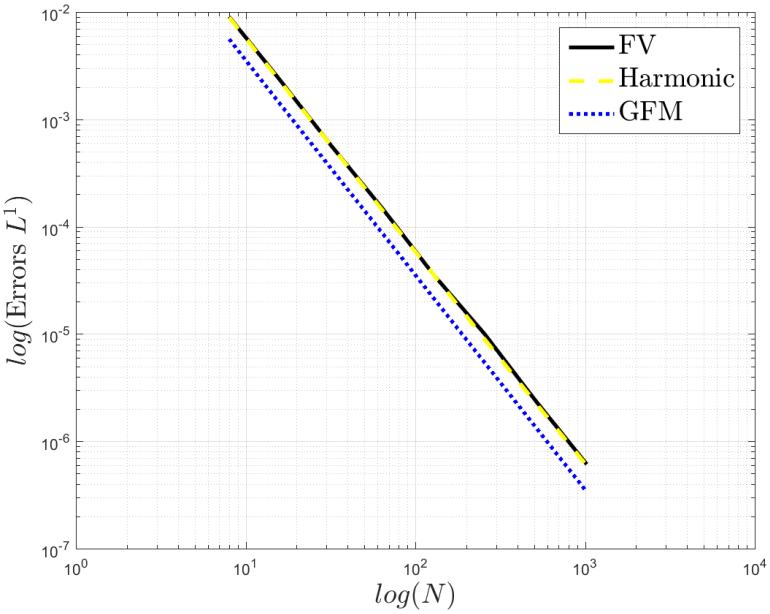

Figure 4.12: ϕ error in the L^1 norm for the 2D MMS validation.

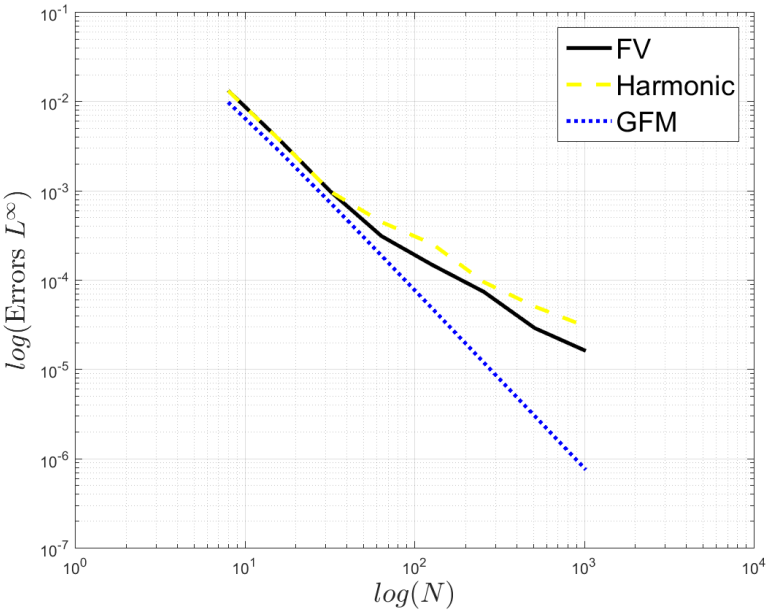

Figure 4.13: ϕ error in the L^∞ norm for the 2D MMS validation.

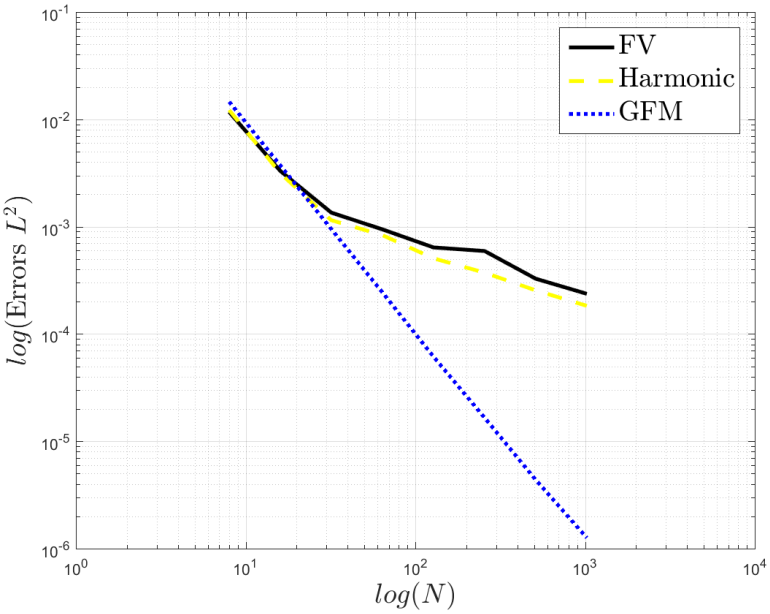

Figure 4.14: E_y error in the L^2 norm for the 2D MMS validation.

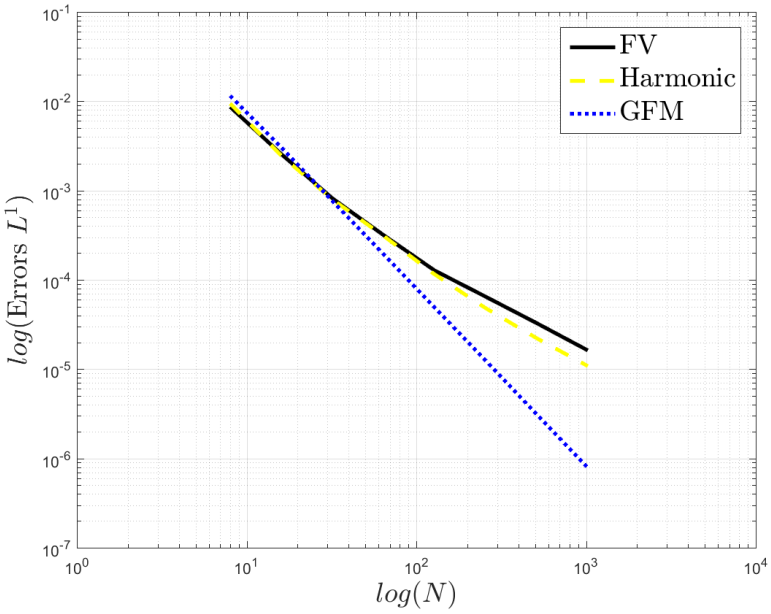

Figure 4.15: E_y error in the L^1 norm for the 2D MMS validation.

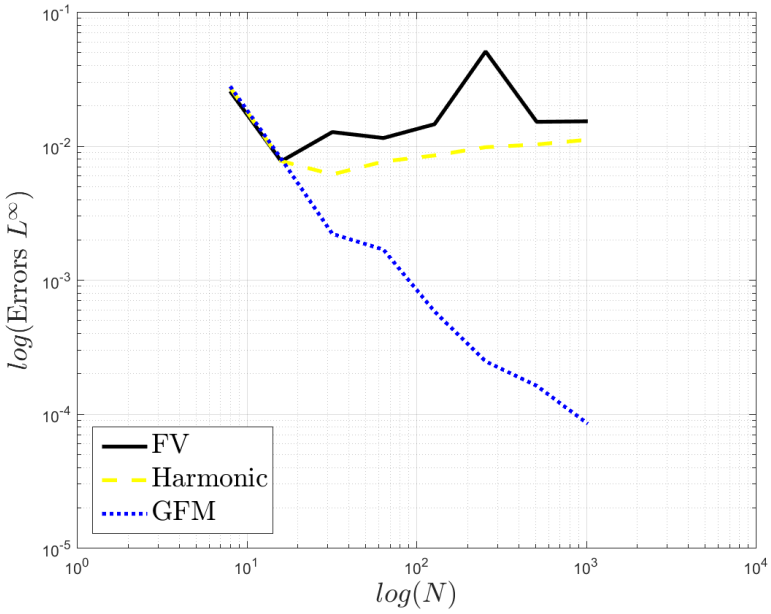

Figure 4.16: E_y error in the L^1 norm for the 2D horizontal MMS validation.

As we can conclude from these, the three schemes being studied have the same error behaviour in the L^2 and L^1 for the potential, with second order accuracy, but the error in the L^∞ norm shows better behaviour for the GFM method, which has second order accuracy, compared to the harmonic scheme and the new finite volume scheme, which has approximately first order accuracy.

Regarding the electric field, the GFM outperforms the other two methods, with second order convergence in the L^2 and L^1 norms, compared to the first order accuracy of the harmonic averaging and the finite volume method. However, the error did not decrease with decreasing grid size in the L^∞ norm. The lack of convergence for the Finite Volume Scheme and the Harmonic scheme is due to the fact that these two methods use the volume of fluid in a given cell to compute derivatives, instead of the distance to the interface, which the GFM uses. The former has been shown to misinterpret the fluid phase more frequently than the latter, which is key to the calculation of the electric field $\mathbf{E}$.

4.2.2 Dielectric rod in a uniform electric field

Further validation of the code can be done through the study of a dielectric rod placed in a uniform electric field, given by the following schematic shown in Fig. 4.17.

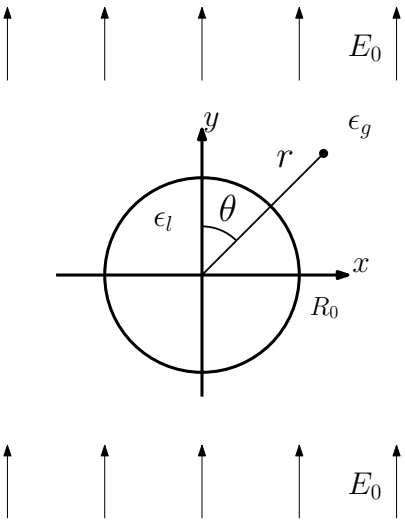

Figure 4.17: Dielectric rod placed in a uniform electric field.

The analytical solution for the potential and the electric field according to the coordinate system is,

$$\phi(r,\theta) = \begin{cases} \frac{-2}{\epsilon_r+1} E_0 r\cos\theta & \text{if } r < R_0, \\ -R_0 E_0 r\cos\theta\left[\frac{r}{R_0} - \frac{R_0}{r}\frac{\epsilon_r-1}{\epsilon_r+1}\right] & \text{if } r \geq R_0, \end{cases} \tag{4.6}$$

$$\mathbf{E}(r,\theta) = \begin{cases} \frac{2}{\epsilon_r+1} E_0 r\,(\cos\theta\mathbf{e}_r - \sin\theta\mathbf{e}_\theta) & \text{if } r < R_0, \\ E_0\cos(\theta)\left[1+\left(\frac{R_0}{r}\right)^2\frac{\epsilon_r-1}{\epsilon_r+1}\right]\mathbf{e}_r + & \\ E_0\sin\theta\left[-1+\left(\frac{R_0}{r}\right)^2\frac{\epsilon_r-1}{\epsilon_r+1}\right]\mathbf{e}_\theta & \text{if } r \geq R_0. \end{cases} \tag{4.7}$$

The simulations were performed for $\epsilon_l = 10\epsilon_0$, $\epsilon_g = \epsilon_0$, $R_0 = 0.1\ m$, $\gamma = 0.32\ J/m^2$ and an electric capillary number number, which gives the relative strength of electric stresses and surface tension, $Ca_{EHD} = \epsilon_g E_0^2 R_0/\gamma = 0.33$. The computational domain had a total size of $L_x \times L_y = 10R_0 \times 20R_0$. If we consider the field along the polar ($\theta = 0°$) and equatorial ($\theta = 90°$) directions, the field is along the normal or tangential component respectively, and in this case is given by the y-component E_y of the electric field. The images shown in Figs. 4.18 and 4.19

give a qualitative comparison between the GFM, FV and CSF methods for the electric field along these directions.

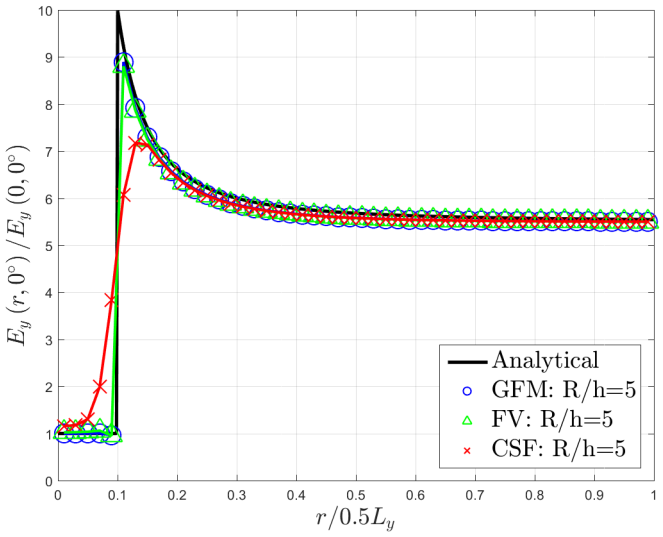

Figure 4.18: Electric field E_y along $\theta = 0°$ for dielectric rod (GFM vs.FV).

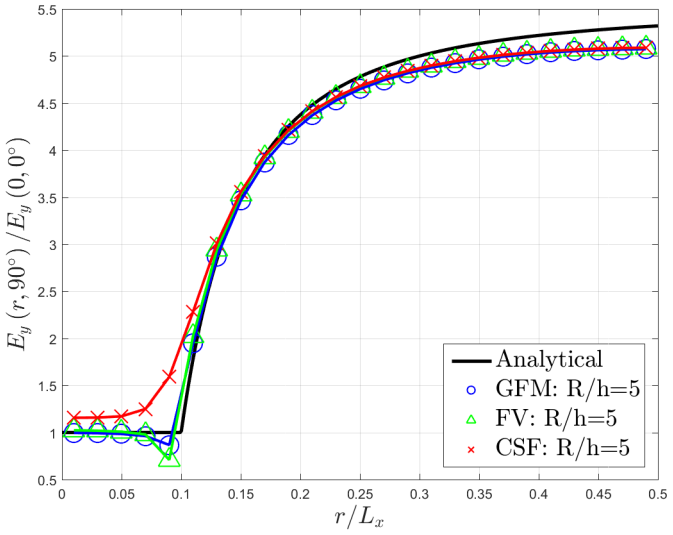

Figure 4.19: Electric field E_y along $\theta = 90°$ for dielectric rod (GFM vs.FV).

Both the jump-preserving methods (GFM and FV) provide a crisp representation of the interface, although it should be noted that the FV performs slightly better for the field right at the interface in the polar direction, while GFM does a better job at the interface for the equatorial direction. It should be noted that the field in the equatorial does not reach the analytical solution as the radius increases in Fig. 4.19 due to the fact that we are imposing symmetry conditions along the z-direction in the simulations, a subtle difference that is not considered in the analytical solution. As was shown in the 1D validation case, the CSF approach smears out the electric field in both of these directions.

The percentage errors being committed for the FV method for the tangential and normal components of the electric can be seen in the following colormap in Fig. 4.20, while the same errors can be seen in Fig. 4.21 for the CSF implementation.

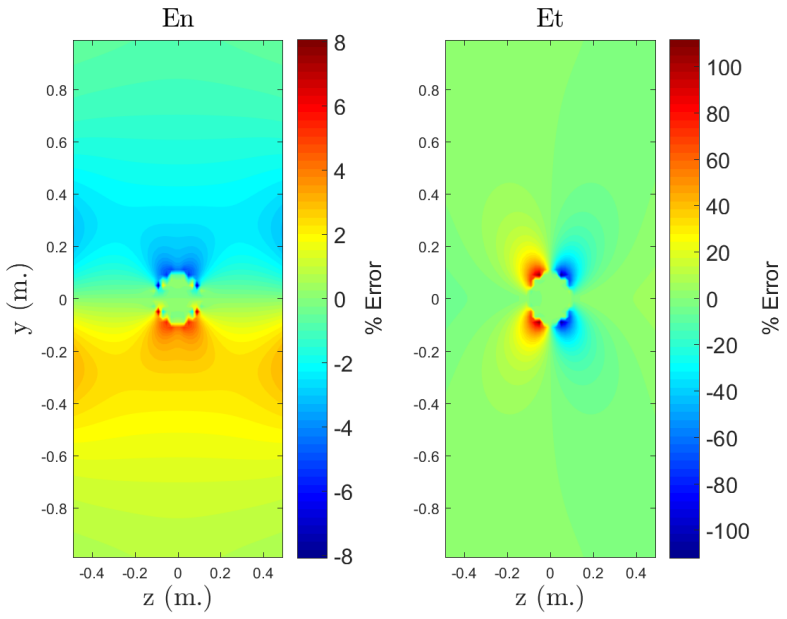

Figure 4.20: Percentage error for the normal (left) and tangential (right) component of the electric field using the FV method.

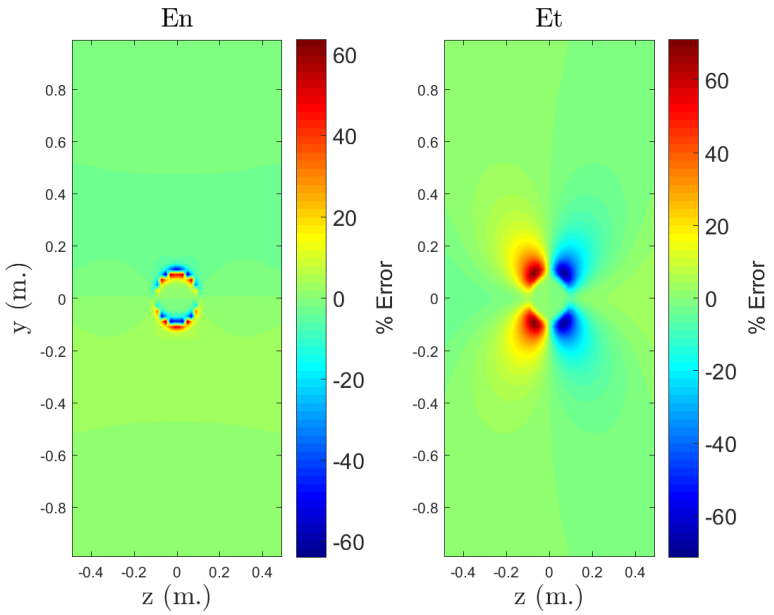

Figure 4.21: Percentage error for the normal (left) and tangential (right) component of the electric field using the CSF approach.

As can be seen in Fig. 4.20 the results for the normal electric field have a maximum absolute percentage error of 8% in the GFM approach, while for the tangential field, the value is around 100%. The reason for this high error in the tangential electric field is due to the assumption given in Eq. 3.4, which states that $[\epsilon E_t]_\Gamma = 0$, which is not true. We must remember, nevertheless that this allowed us to decouple the directions when constructing our discretization, and that if this assumption was not made, the computational stencil to discretize the derivatives would need to make use of 27 points in three dimensions, considerably raising the cost of these simulations.

On the other hand, we can observe in Fig. 4.21 that the maximum absolute percentage error in the CSF for the tangential and normal electric field is around 60%, due to the smeared out nature of the methodology.

Due to the high errors being committed for the tangential electric field, it is of prime importance to be able to gauge the relative size of the normal component of the electric field, relative to the modulus of the total electric field, in order to be able to determine the regions of the problem where the condition given by Eq. 3.4 is not verified. This comparison can be found in Fig. 4.22.

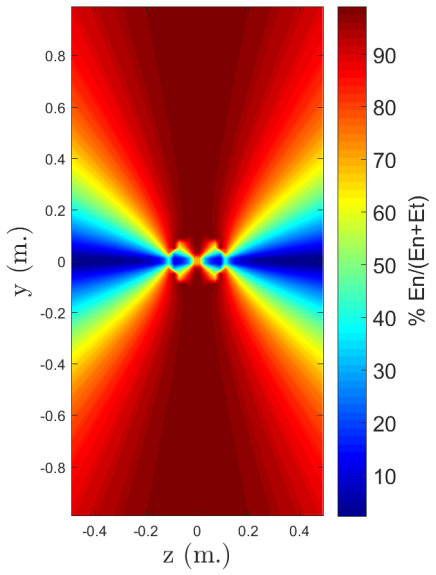

Figure 4.22: Percentage of the normal electric field with respect to the total electric field for the dielectric rod.

Due to the dielectric nature of both of the fluids, the effects of the electric field will be felt in the pressure difference that the quiescent drop experiences, given by Eq. 2.35, which in our case, given the curvature of the cylinder will be equal to,

$$\begin{aligned}[p]_\Gamma &= \gamma\kappa + \frac{1}{2}\left[\epsilon \mathbf{E}_n^2\right] - \frac{1}{2}\left[\epsilon \mathbf{E}_{t_i}^2\right] \\ &= \frac{\gamma}{R_0} + \frac{1-\epsilon_r}{2}\left(\frac{2E_0}{\epsilon_r+1}\right)^2\left(\epsilon_l cos^2\theta + \epsilon_g sin^2\theta\right)\end{aligned} \tag{4.8}$$

This pressure contribution from the EHD term will have the shape of a sinu-

soid, which will deform the drop over time and result in a 2D prolate spheroid. Oblate spheroids are not possible given that in order for the drop to deform that way $[p]^{EHD}(\theta = 0°) > [p]^{EHD}(\theta = 90°)$. This leads us to the inequality found in Eq. 4.9.

$$(1 - \epsilon_r)\,\epsilon_l = (1 - \epsilon_r)\,\epsilon_g \tag{4.9}$$

If we assume that $\epsilon_r < 1$ and we eliminate the $1 - \epsilon_r$ term, we arrive at $\epsilon_l/\epsilon_g > 1$, which is compatible with the first condition, since $\epsilon_r = \epsilon_l/\epsilon_r$. Similarly, assuming that $\epsilon_r > 1$ leads to $\epsilon_l/\epsilon_g < 1$ following a similar procedure. Since both the assumptions lead to contradictory conditions, the oblate 2D spheroid cannot be physically obtained for a dielectric rod.

The images found in Figs. 4.23, 4.25, 4.29 and 4.27 shows a comparison of the pressure jump obtained with the GFM and the analytical solution, under three different levels of refinement, given by 5, 10 and 20 cells per radius (CPR). Due to the symmetry of the pressure jump with respect to the equator, only angles comprehended between 0° and 90° are shown.

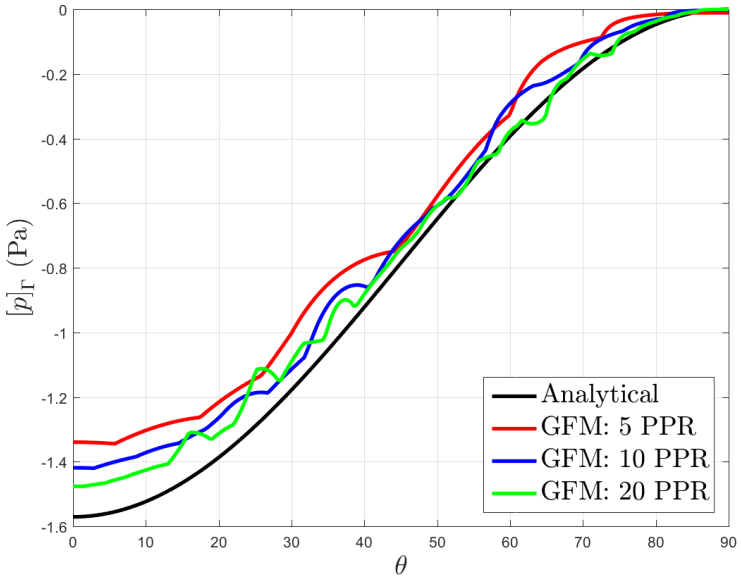

Figure 4.23: $[p]_\Gamma$ due to the electric field along the normal direction for a dielectric rod (GFM).

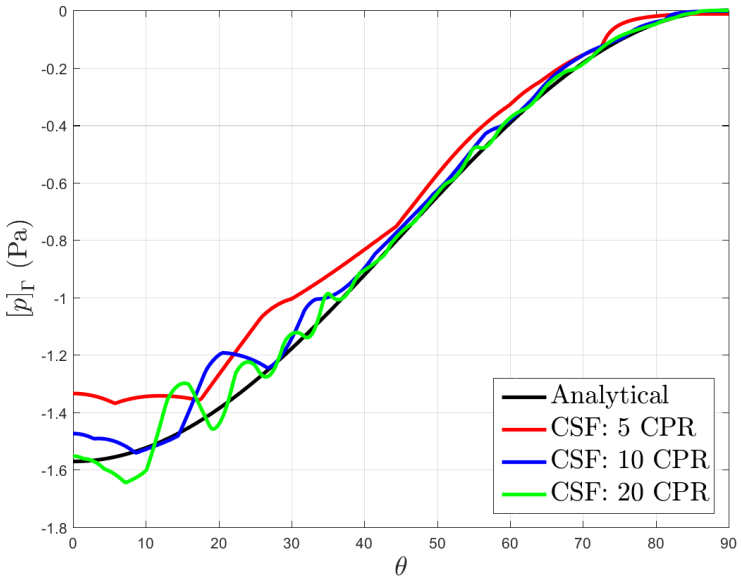

Figure 4.24: $[p]_\Gamma$ due to the electric field along the normal direction for a dielectric rod (CSF).

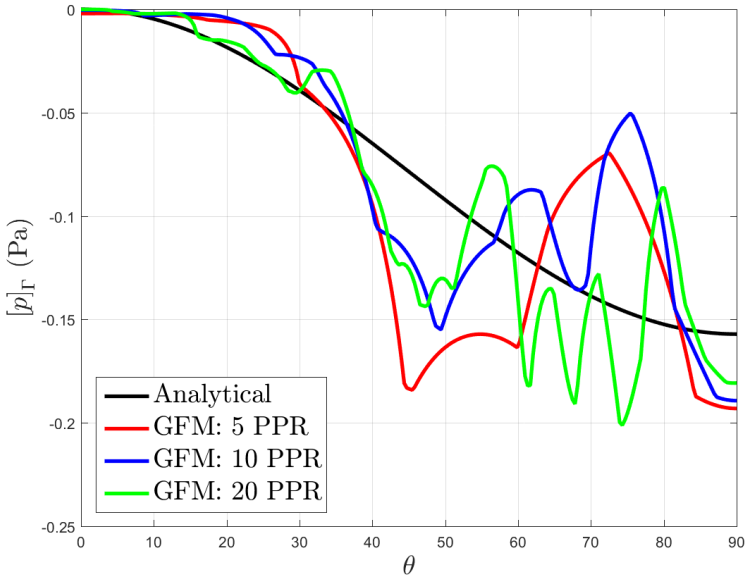

Figure 4.25: $[p]_\Gamma$ due to the electric field along the tangential direction for a dielectric rod (GFM).

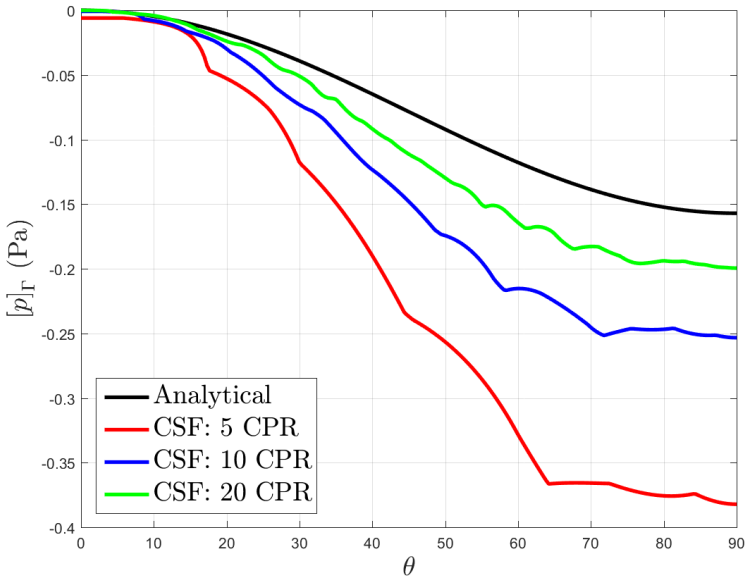

Figure 4.26: $[p]_\Gamma$ due to the electric field along the tangential direction for a dielectric rod (CSF).

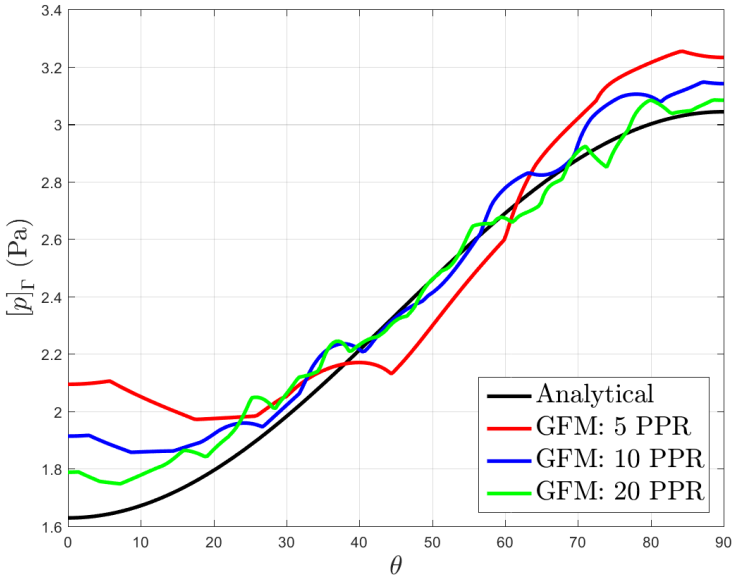

Figure 4.27: Total $[p]_\Gamma$ due to the electric and surface tension effects for a dielectric rod (GFM).

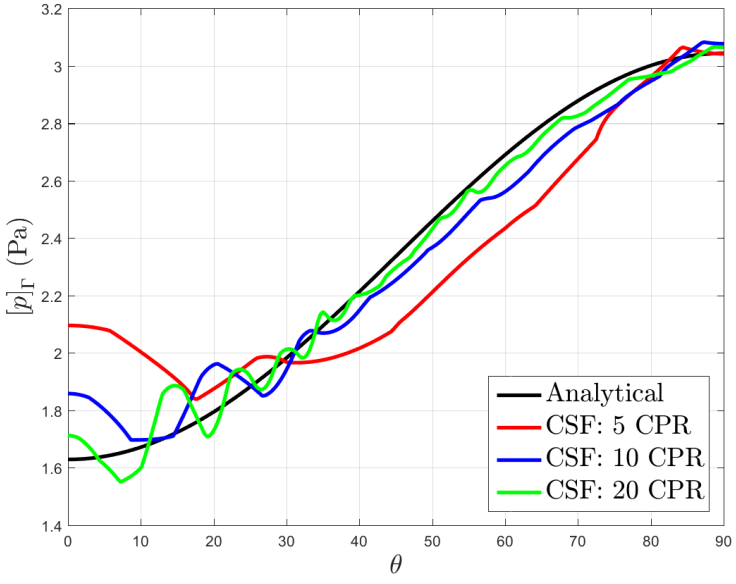

Figure 4.28: $[p]_\Gamma$ due to the electric field along the tangential direction for a dielectric rod (CSF).

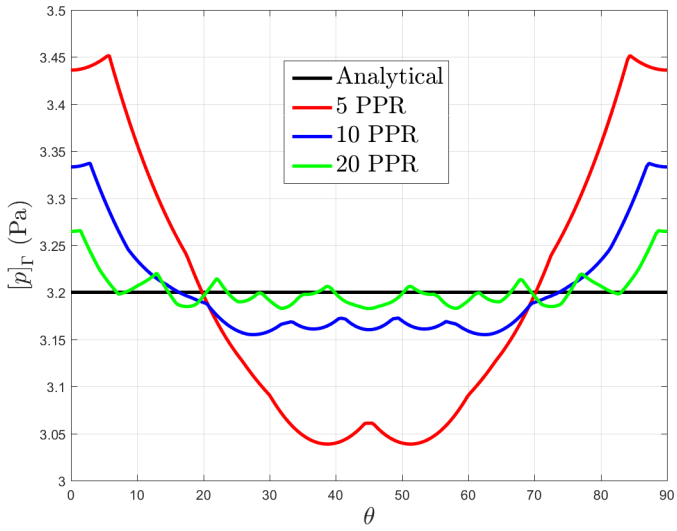

Figure 4.29: Pressure jump [p] due to surface tension versus angle for a dielectric rod.

We can see in Figs. 4.23 and 4.24 that with a coarse mesh of 5 cells per radius (CPR) we are able to obtain good agreement with the analytical expression for the pressure jump component caused by the normal electric field for both the approaches. We can also see that the greatest errors are being made in the vicinity of the pole of the rod, with a percentage error for $\theta = 0°$ of 14.70% for 5 CPR and of 5.98% for 20 CPR using the GFM method and of 14.95% for 5 CPR and of 1.14% for 20 CPR using the CSF approach.

Regarding the tangential pressure jump found in Figs. 4.25 and 4.26 the results obtained with the GFM show a highly oscillatory behaviour with percentage errors for $\theta = 90°$ of 22.85% and 15.08% for 5 and 20 CPR. Meanwhile the CSF methodology provides a smoother approach to the analytical solution upon refinmenent, due to its nature, with an absolute percentage error for $\theta = 90°$ of 143.15% and 26.98% for 5 and 20 CPR.

The errors in the jump due to surface tension can be seen in Fig. 4.29, which greatly improve as we refine the mesh from a percentage error of 7.37% to 2.03% as found in $\theta = 90°$.

We can better understand the maximum errors being made in the pressure jumps for the normal and tangential components if we consider the electric field E_y for these two levels of refinement along the polar ($\theta = 0°$ and $\theta = 180°$) and equatorial ($\theta = 90°$) directions, shown in Figs. 4.30 and 4.31.

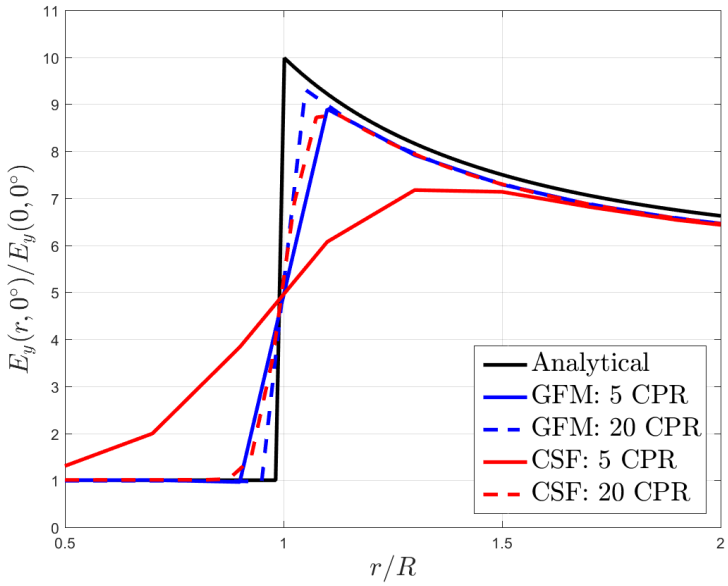

Figure 4.30: Electric field E_y along $\theta = 0°$ for the dielectric rod (5 vs. 20 Cells per radius).

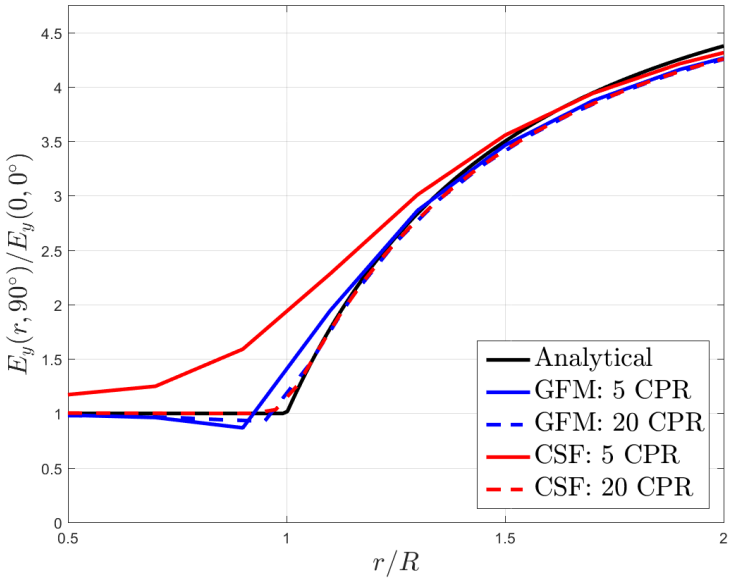

Figure 4.31: Electric field E_y along $\theta = 90°$ for the dielectric rod (5 vs. 20 Cells per radius).

Despite the accuracy of both of the levels of refinement for the electric field, the Table 4.2 shows the percentage errors being made in the vicinity of the interface for the electric, with respect to the true value of the electric field at the interface for the GFM method.

Direction	5 CPR		20 CPR	
	Liquid	Gas	Liquid	Gas
Polar	3.69	10.88	2.85	6.74
Equatorial	13.36	94.63	7.15	43.78

Table 4.2: Percentage error (%) in the electric field in the vicinity of the liquid-gas interface with the GFM.

The point-wise electric field values analysed in the previous table are the ones that will ultimately be used to calculate the pressure jump due to the normal electric field for $\theta = 0°$ and $\theta = 180°$, and the pressure jump due to the

tangential electric field for $\theta = 90°$. If we use these values electric field values to calculate the pressure jump according to Eq. 2.35, we arrive at the following percentage errors, shown in Table4.3 for the pressure jump with respect to the analytical solution.

Direction	5 CPR		20 CPR	
	Liquid	Gas	Liquid	Gas
Polar	7.25	20.87	5.67	13.37
Equatorial	24.82	278.23	13.81	106.68

Table 4.3: Percentage error (%) in the pressure jump in the vicinity of the liquid-gas interface with the GFM method.

The values of the pressure jump are then interpolated to the interface location using values from the liquid and gas phases, which helps us explain the errors found in Figs. 4.23, 4.25, 4.29 and 4.27. We can conclude from Tables 4.2 and 4.3 that the GFM performs better in calculating the normal electric field than the tangential electric field, due to the assumption stated in Eq. 3.4. We can also conclude that a fine grid is needed to accurately describe the pressure jump values in the gas, due to the fact that the field defined by Eqs. 4.7 varies with $\left(\frac{R_0}{r}\right)^2$, and thus if the point in the liquid phase is not close enough to the interface, the value of the jump will not be accurate.

Regarding the evolution of the electric field calculated with the CSF approach and shown in Figs. 4.30 and 4.31, an integration is needed over the transition region to arrive at the value of the pressure jump $[p]_\Gamma$ and thus no explicit analysis of the errors being made on each side of the interface can be made.

A comparison of the total pressure jump at the pole, caused by the normal and tangential electric field and the surface tension for the GFM, FV

and Harmonic Averaging (HA) methods can be seen in Table 4.4, showing an accuracy higher than the one shown by Tomar et al. [19] for the values at the pole using the CSF methodology. The values at the equator have not been compared due to the lack of data for that location.

	Method		
CPR	GFM	FV	HA
5	2.60	2.47	2.16
10	2.33	2.82	2.56
20	1.16	1.69	2.39

Table 4.4: Error (%) in the calculation of the total pressure jump $[p]$ at the pole.

A graphical comparison of the deviation from the exact pressure jump with respect to the analytical solution can be seen in Figs. 4.32 and 4.33 for the GFM and FV discretizations.

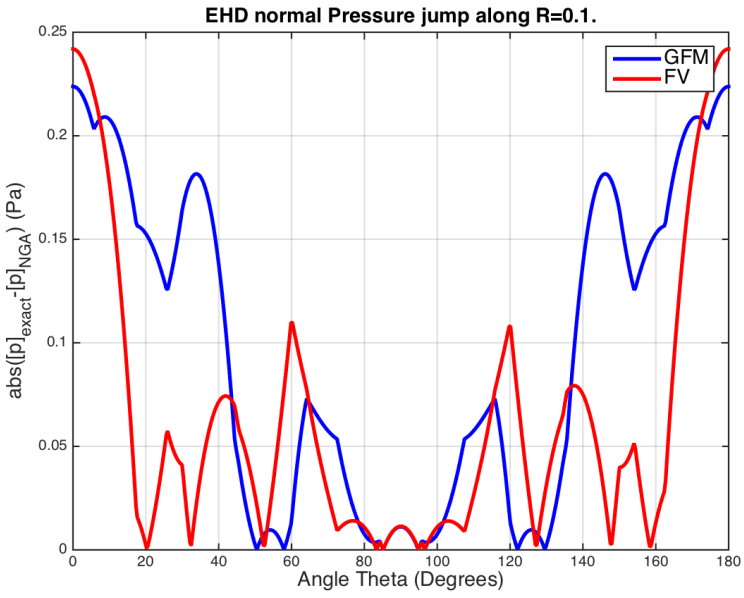

Figure 4.32: Deviation from the analytical solution for the jump due to the normal field (GFM vs. FV).

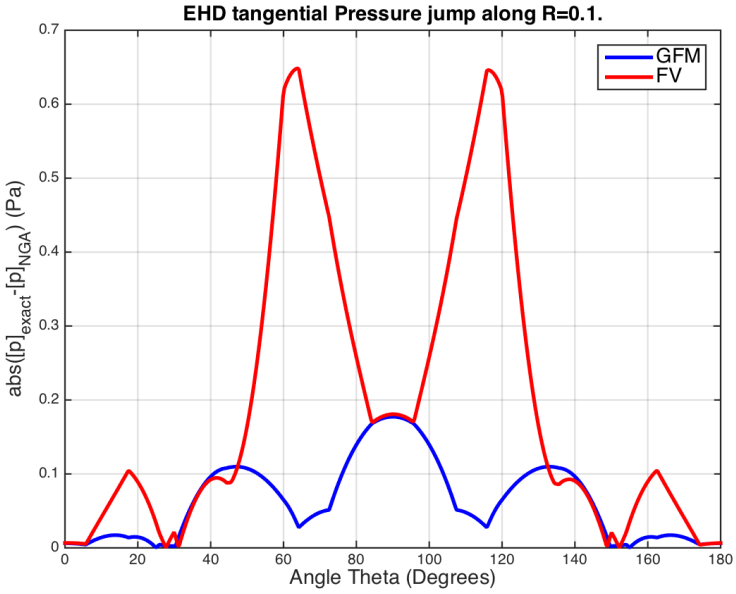

Figure 4.33: Deviation from the analytical solution for the jump due to the tangential field (GFM vs. FV).

4.3 3D Study

4.3.1 Dielectric drop in a uniform electric field

The following test case involves the simulation of a three dimensional spherical liquid drop placed in a uniform electric field inside a gas. This case is of special interest, due to the importance of this geometric shape in atomization processes. The problem schematic is shown in Fig. 4.34. The solution to this problem can be found in classical electromagnetism textbooks, such as Griffiths, Landau and Jackson [20, 23, 35] .

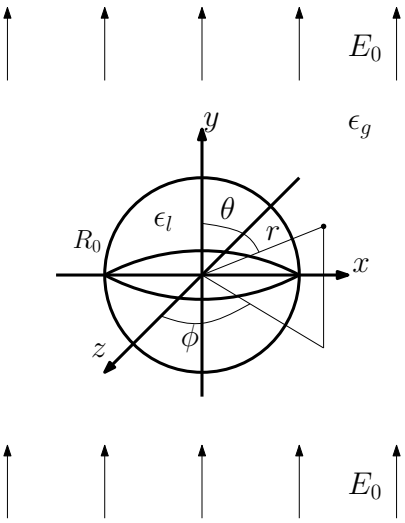

Figure 4.34: Spherical liquid drop suspended in a gas and subject to an electric field E_0.

The potential has the expression given in Eq. 4.10, while the electric field, at which we arrive once we take the gradient is given by Eq. 4.11.

$$\phi(r,\theta) = \begin{cases} \frac{-3}{\epsilon_r+2} E_0 r \cos\theta & \text{if } r < R_0, \\ -E_0 r \cos\theta + \frac{\epsilon_r-1}{\epsilon_r+2} E_0 \left(\frac{R_0}{r}\right)^3 \sin\theta & \text{if } r \geq R_0, \end{cases} \tag{4.10}$$

$$\mathbf{E}(r,\theta) = \begin{cases} \frac{3}{\epsilon_r+2} E_0 r \left(\cos\theta \mathbf{e}_r - \sin\theta \mathbf{e}_\theta\right) & \text{if } r < R_0, \\ E_0 \cos\theta \left[1 + 2\left(\frac{R_0}{r}\right)^3 \frac{\epsilon_r-1}{\epsilon_r+2}\right] \mathbf{e}_r + & \\ E_0 \sin\theta \left[-1 + \left(\frac{R_0}{r}\right)^3 \frac{\epsilon_r-1}{\epsilon_r+2}\right] \mathbf{e}_\theta & \text{if } r \geq R_0. \end{cases} \tag{4.11}$$

The simulations were performed for $\epsilon_l = 10\epsilon_0$, $\epsilon_g = \epsilon_0$, $R_0 = 0.1\ m$, $\gamma = 0.32\ J/m^2$ and an electric capillary number number $Ca_{EHD} = \epsilon_g E_0^2 R_0/\gamma = 0.33$. As with the dielectric rod, the electrostatic effects in out case are coupled to the fluid mechanics through the pressure jump felt at the liquid-gas interphase, which has follows the evolution found in Eq. 4.12. The domain has a size $L_x \times L_y \times L_z = 10R_0 \times 20R_0 \times 10R_0$. As with the dielectric rod validation case, the physical system will only evolve to a prolate spheroid over time, and not an oblate spheroid,

with a pressure jump given by Eq. 4.12.

$$
\begin{aligned}
[p]_\Gamma &= \gamma\kappa + \frac{1}{2}\left[\epsilon \mathbf{E}_n^2\right] - \frac{1}{2}\left[\epsilon \mathbf{E}_{t_i}^2\right] \\
&= \frac{2\gamma}{R_0} + \frac{1-\epsilon_r}{2}\left(\frac{3E_0}{\epsilon_r+2}\right)^2 \left(\epsilon_l cos^2\theta + \epsilon_g sin^2\theta\right)
\end{aligned}
\tag{4.12}
$$

The images shown in Figs. 4.35, 4.37, 4.39 and 4.41 depict the pressure jump due to the various effects found above, namely E_n, E_t and surface tension along two different ϕ angles, given by $\phi = 0°$ and $\phi = 45°$. The jump preserving methods (FV and GFM) are grouped into a single figure, while the results obtained with the CSF methodology are presented below the latter.

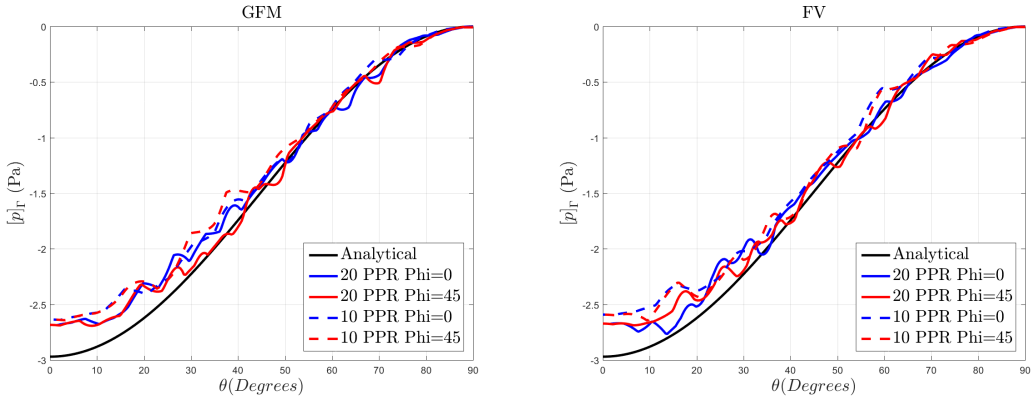

(a) GFM (b) FV

Figure 4.35: $[p]_\Gamma$ due to the normal electric field $\mathbf{E}_n$ for the spherical drop (FV & GFM).

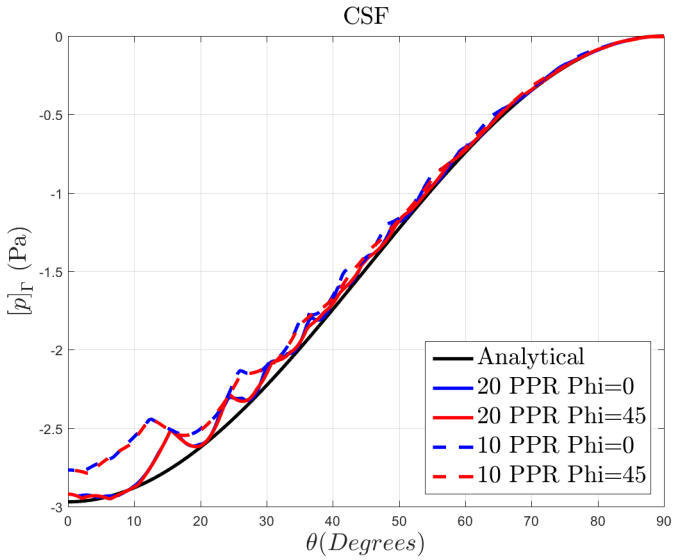

Figure 4.36: $[p]_\Gamma$ due to the normal electric field $\mathbf{E}_n$ for the spherical drop (CSF).

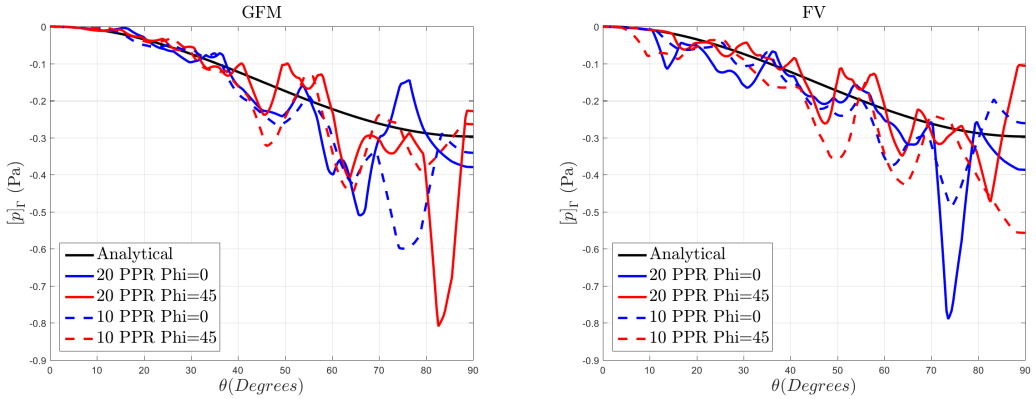

(a) GFM (b) FV

Figure 4.37: $[p]_\Gamma$ due to the normal electric field $\mathbf{E}_t$ for the spherical drop (FV & GFM).

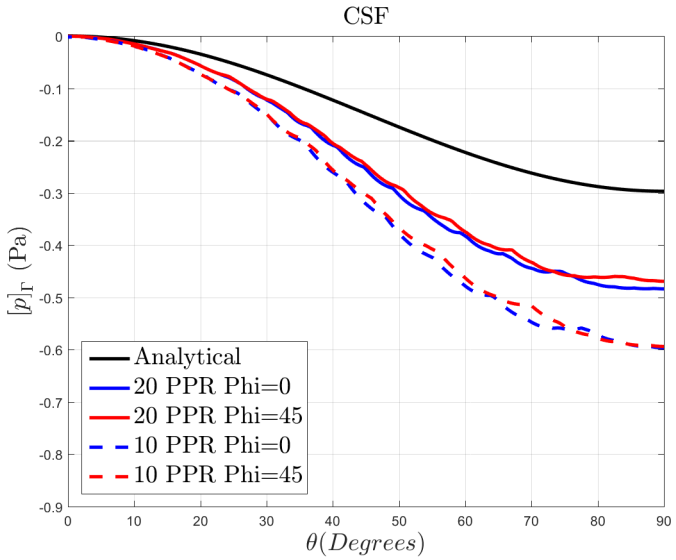

Figure 4.38: $[p]_\Gamma$ due to the normal electric field $\mathbf{E}_t$ for the spherical drop (CSF).

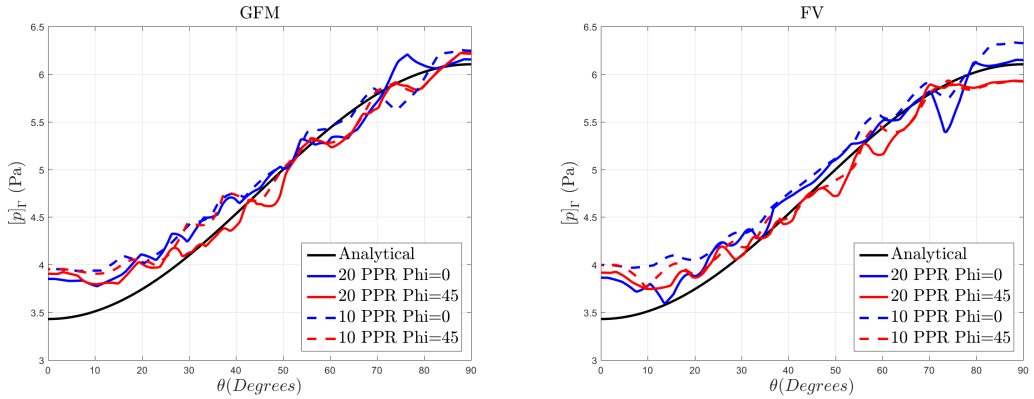

(a) GFM (b) FV

Figure 4.39: Total $[p]_\Gamma$ due to electric and surface tension effects for the spherical drop (FV & GFM).

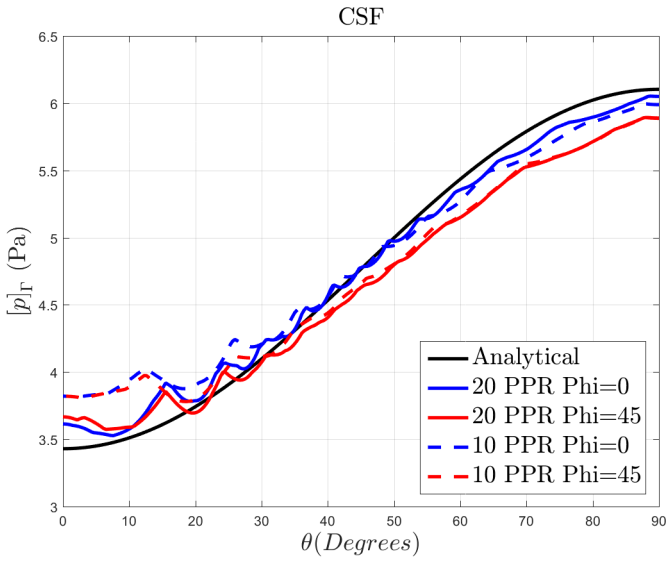

Figure 4.40: Total $[p]_\Gamma$ due to electric and surface tension effects for the spherical drop (CSF).

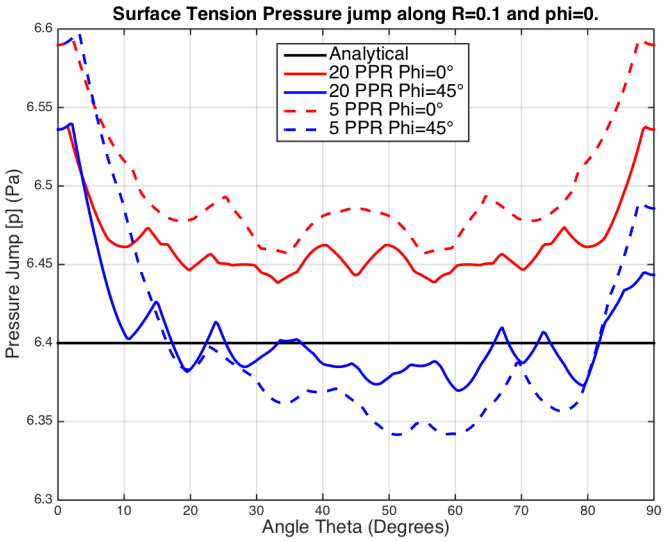

Figure 4.41: Total $[p]_\Gamma$ due to surface tension effects for the spherical drop (CSF).

As was seen in with the dielectric rod, the three methods provide good results for the EHD pressure jump caused by E_n, as is seen in Figs. 4.35 and 4.3.1. On the other hand, the jump due to E_t does not converge smoothly to the solution, as Fig. 4.37 shows, while the CSF approach does not suffer from this problem, as seen in Fig. 4.3.1.

An interesting analysis of the behaviour of the pressure jump calculation can be made by studying the behaviour of the errors with respect to the spherical coordinate angles θ and ϕ. The Figs. 4.42, 4.43 and 4.44 show the variation of the pressure jump due to the normal electric field, as the previous angles vary, for the points inside and outside of the drop, and also for the algorithm that is implemented in NGA, which uses both points inside and outside of the drop.

The symmetry of the operators and the system is apparent in the fig-

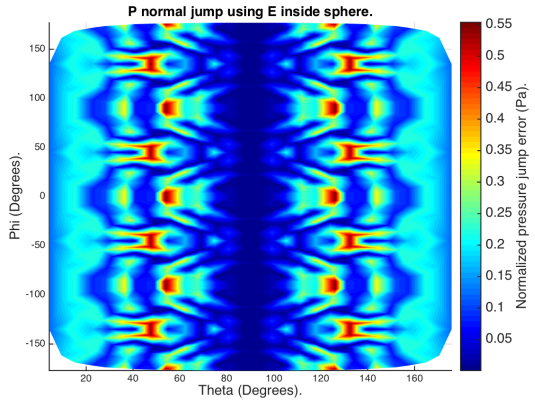

(a) Points inside the drop.

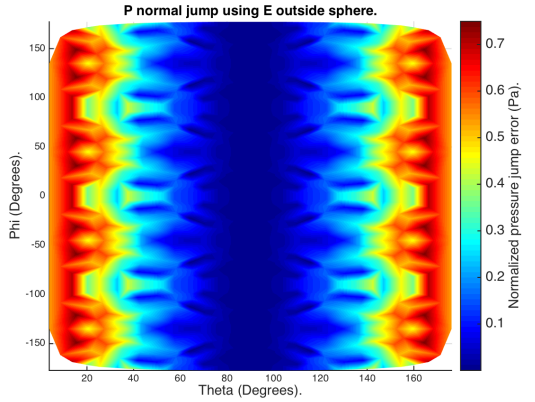

(b) Points outside the drop.

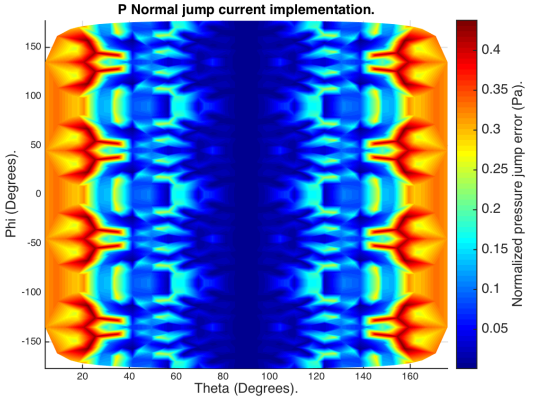

(c) NGA Algorithm

Figure 4.42: Absolute error comparison in the pressure jump $[p]$ due to the normal electric field E_n for the dielectric drop.

ures, as the Cartesian discretization with square volume cells is symmetric with respect to the $x-y$, the $x-z$ and $y-z$ plane. It is also easy to see straight away that the error in the L^{∞} norm is lowest in the current scheme being implemented in NGA, which makes use of points both inside and outside the drop. The points inside the drop, as seen in Fig. 4.42(a), perform better than the ones outside the sphere, as seen in Fig. 4.42(b), for θ angles between $0^{\circ} - 40^{\circ}$ and 140°-180° but using points outside of the drop provides better results for the range of angles $40^{\circ} - 140^{\circ}$. The pressure jump implemented in NGA, in Fig. 4.42(c), uses points both inside and outside, weighted according to the distance to the interface, and thus provides a reasonable compromise. As was made evident by Figs. 4.35, 4.37, 4.39 and 4.41, the mesh used creates a pressure jump dependent on the angle ϕ, this is to be expected given our 3D stencil, despite the fact that Eq. 4.12 is independent of ϕ.

Examining the errors in the pressure jump $[p]$ due to the tangential electric field E_t, we can see that both for the points inside in Fig. 4.43(a) and outside the drop in Fig. 4.43(b), there is a θ range given by the angles $60^{\circ} - 120^{\circ}$ where the greatest parts of the error are concentrated, albeit the fact that the errors for the points inside the drop are much smaller than for the points outside. In this case, as was mentioned earlier, the errors in the pressure jump $[p]$ due to the tangential electric field E_t are much larger compared to the magnitude of this specific pressure jump, due to the fact that we assumed that $[\epsilon \mathbf{E}]_{\Gamma} \approx [\epsilon E_n]_{\Gamma}$.

Observing the data for depicted in Figs. 4.44(a) and 4.44(b), the cumulative effects of pressure jumps is seen, and we can see that for the points inside 4.44(b) we perform better in the θ range given by $40^{\circ} - 6^{\circ}$ and $120^{\circ} - 140^{\circ}$, while the points inside the drop in Fig. 4.44(b) present lower errors everywhere

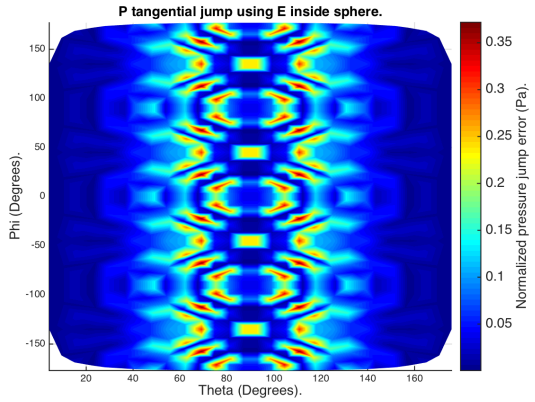

(a) Points inside the drop.

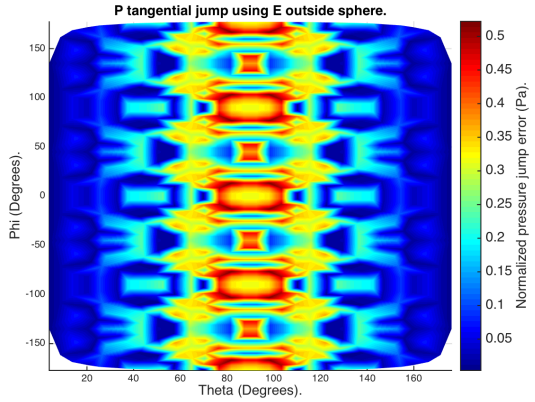

(b) Points outside the drop.

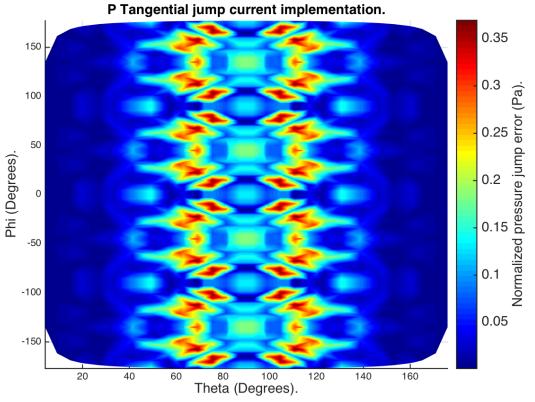

(c) NGA Algorithm

Figure 4.43: Absolute error comparison in the pressure jump $[p]$ due to the tangential electric field E_t for the dielectric drop.

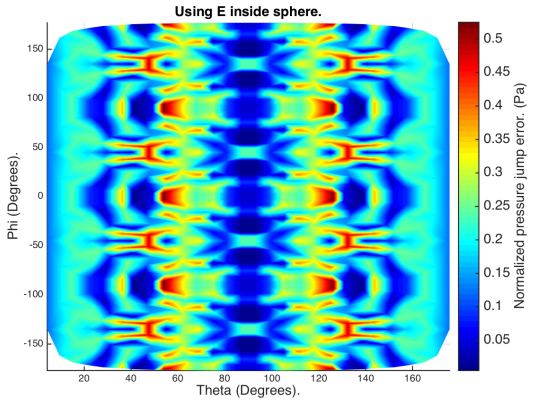

(a) Points inside the drop.

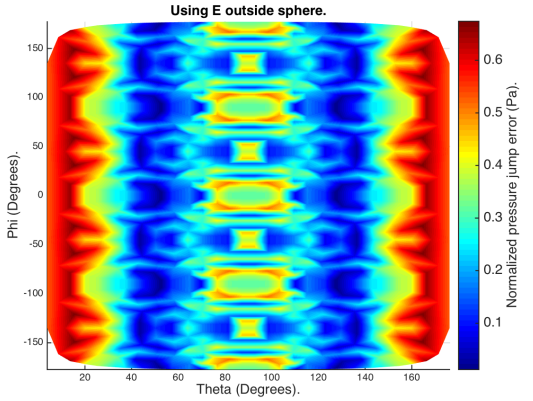

(b) Points outside the drop.

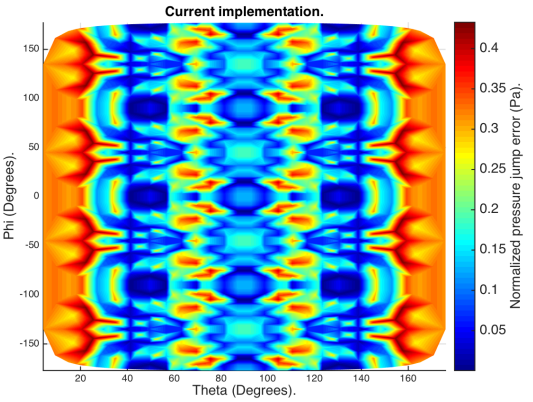

(c) NGA Algorithm

Figure 4.44: Absolute error comparison in the pressure jump $[p]$ due to the normal(E_n) and tangential E_t electric field for the dielectric drop.

else. Notable is the fact that the algorithms implemented in NGA give rise to a dependence with respect to ϕ that does not appear in our physical phenomenon.

CHAPTER 5

CONCLUSIONS AND PERSPECTIVES

The accuracy of a popular jump-preserving method, known as the Ghost Fluid Method (GFM), for the resolution of the Poisson equation has been characterized and compared to a novel Finite Volume (FV) method, to a simple method of harmonic averaging of coefficients and to a smeared out Continuum Surface Force (CSF) approach, first used to model surface tension by Brackbill et al. [32].

The results were compared to the work by Tomar et al. [19], who used the CSF approach to solve several analytical problems in electrohydrodynamics. The jump-preserving methods showed better accuracy for coarse mesh resolutions, but experienced oscillatory behaviour with grid refinement for the pressure jump caused by tangential electric field components. This could be partly due to the nature of the method used, and to the fact that unlike Tomar et al. who used an axisymmetric discretization of operators, a more general Cartesian one was used for this present work.

In order to improve the accuracy of the method, a jump-preserving approach could be used for the normal electric field E_n effects, which showed good accuracy, and a CSF approach for the tangential electric field effects E_t, to try to limit the oscillations experienced.

The next logical step in validation would be to model the three-dimensional deformation of a dielectric drop in an electric field, whose deformation can be compared to the analytical formula derived by Taylor [10], where surface tension, EHD and viscous stresses deform the drop until the equilibrium

is reached.

An accurate set of tools for the resolution of EHD problems will give valuable insight to topics such as electric field induced turbulence, or the role of electric fields in atomization.

BIBLIOGRAPHY

[1] Lord Rayleigh. Xx. on the equilibrium of liquid conducting masses charged with electricity. *The London, Edinburgh, and Dublin Philosophical Magazine and Journal of Science*, 14(87):184–186, 1882.

[2] J. Zeleny. The electrical discharge from liquid points, and a hydrostatic method of measuring the electric intensity at their surfaces. *Physical Review*, 3(2):69, 1914.

[3] T. R. Wilson and G. I. Taylor. The bursting of soap-bubbles in a uniform electric field. In *Mathematical Proceedings of the Cambridge Philosophical Society*, volume 22, pages 728–730. Cambridge Univ Press, 1925.

[4] J. J. Nolan. The breaking of water-drops by electric fields. In *Proceedings of the Royal Irish Academy. Section A: Mathematical and Physical Sciences*, volume 37, pages 28–39. JSTOR, 1924.

[5] W. A. Macky. Some investigations on the deformation and breaking of water drops in strong electric fields. *Proceedings of the Royal Society of London. Series A, Containing Papers of a Mathematical and Physical Character*, 133(822):565–587, 1931.

[6] G. I. Taylor. Disintegration of water drops in an electric field. In *Proceedings of the Royal Society of London A: Mathematical, Physical and Engineering Sciences*, volume 280, pages 383–397. The Royal Society, 1964.

[7] R. S. Allan and S. G. Mason. Particle behaviour in shear and electric fields. deformation and burst of fluid drops. In *Proceedings of the Royal Society of London A: Mathematical, Physical and Engineering Sciences*, volume 267, pages 45–61. The Royal Society, 1962.

[8] J. R. Melcher and G. I. Taylor. Electrohydrodynamics: a review of the role of interfacial shear stresses. *Annual Review of Fluid Mechanics*, 1(1):111–146, 1969.

[9] D. A. Saville. Electrohydrodynamics: the taylor-melcher leaky dielectric model. *Annual review of fluid mechanics*, 29(1):27–64, 1997.

[10] G. I. Taylor. Studies in electrohydrodynamics. i. the circulation produced in a drop by electrical field. In *Proceedings of the Royal Society of London A:*

Mathematical, Physical and Engineering Sciences, volume 291, pages 159–166. The Royal Society, 1966.

[11] P. F. Salipante and P. M. Vlahovska. Electrohydrodynamics of drops in strong uniform dc electric fields. *Physics of Fluids (1994-present)*, 22(11):112110, 2010.

[12] P. F. Salipante and P. M. Vlahovska. Electrohydrodynamic rotations of a viscous droplet. *Physical Review E*, 88(4):043003, 2013.

[13] O. Vizika and D. A. Saville. The electrohydrodynamic deformation of drops suspended in liquids in steady and oscillatory electric fields. *Journal of fluid Mechanics*, 239:1–21, 1992.

[14] H. Oğuz and J. Zeng. Axisymmetric and three-dimensional boundary integral simulations of bubble growth from an underwater orifice. *Engineering analysis with boundary elements*, 19(4):319–330, 1997.

[15] J. D. Sherwood. Breakup of fluid droplets in electric and magnetic fields. *Journal of Fluid Mechanics*, 188:133–146, 1988.

[16] J. C. Baygents, N. J. Rivette, and H. A. Stone. Electrohydrodynamic deformation and interaction of drop pairs. *Journal of Fluid Mechanics*, 368:359–375, 1998.

[17] F. J. Higuera. Injection of bubbles in a quiescent inviscid liquid under a uniform electric field. *Journal of Fluid Mechanics*, 568:203–222, 2006.

[18] R. T. Collins, M. T. Harris, and O. A. Basaran. Breakup of electrified jets. *Journal of Fluid Mechanics*, 588:75–129, 2007.

[19] G. Tomar, D. Gerlach, G. Biswas, N. Alleborn, A. Sharma, F. Durst, S. W. J. Welch, and A. Delgado. Two-phase electrohydrodynamic simulations using a volume-of-fluid approach. *Journal of Computational Physics*, 227(2):1267–1285, 2007.

[20] L. D. Landau and E. M. Lifshitz. *Electrodynamics of Continuous Media*, volume 8 of *Course of Theoretical Physics*. Pergamon, second edition edition, 1865.

[21] J. R. Melcher. *Continuum electromechanics*, volume 2. MIT press Cambridge, 1981.

[22] J. A. Stratton. *Electromagnetic theory*. John Wiley & Sons, 2007.

[23] D. J. Griffiths. *Introduction to electrodynamics*, volume 3. Prentice Hall Upper Saddle River, NJ, 1999.

[24] O. Desjardins, G. Blanquart, G. Balarac, and H. Pitsch. High order conservative finite difference scheme for variable density low mach number turbulent flows. *Journal of Computational Physics*, 227(15):7125–7159, 2008.

[25] O. Desjardins, V. Moureau, and H. Pitsch. An accurate conservative level set/ghost fluid method for simulating turbulent atomization. *Journal of Computational Physics*, 227(18):8395–8416, 2008.

[26] O. Desjardins and H. Pitsch. A spectrally refined interface approach for simulating multiphase flows. *Journal of Computational Physics*, 228(5):1658–1677, 2009.

[27] C. D. Pierce and P. Moin. Progress-variable approach for large-eddy simulation of non-premixed turbulent combustion. *Journal of Fluid Mechanics*, 504:73–97, 2004.

[28] B. P. Van Poppel, O. Desjardins, and J. W. Daily. A ghost fluid, level set methodology for simulating multiphase electrohydrodynamic flows with application to liquid fuel injection. *Journal of Computational Physics*, 229(20):7977–7996, 2010.

[29] J. E. Dendy. Black box multigrid. *Journal of Computational Physics*, 48(3):366–386, 1982.

[30] R. P. Fedkiw, T. Aslam, B. Merriman, and S. Osher. A non-oscillatory eulerian approach to interfaces in multimaterial flows (the ghost fluid method). *Journal of computational physics*, 152(2):457–492, 1999.

[31] X. Liu, R. P. Fedkiw, and M. Kang. A boundary condition capturing method for poisson's equation on irregular domains. *Journal of computational Physics*, 160(1):151–178, 2000.

[32] J. U. Brackbill, D. B. Kothe, and C. Zemach. A continuum method for modeling surface tension. *Journal of computational physics*, 100(2):335–354, 1992.

[33] E. Olsson and G. Kreiss. A conservative level set method for two phase flow. *Journal of computational physics*, 210(1):225–246, 2005.

[34] E. Olsson, G. Kreiss, and S. Zahedi. A conservative level set method for two phase flow ii. *Journal of Computational Physics*, 225(1):785–807, 2007.

[35] D. J. Jackson. *Classical electrodynamics*. John Wiley & Sons, Inc., New York, NY, 1999.